Chapter 4

A 94-GHz Frequency Modulation Continuous Wave Radar Imaging and Motion Compensation

Jiwoong Yu, Sumin Kim and Min-Ho Ka

Additional information is available at the end of the chapter

http://dx.doi.org/10.5772/intechopen.74692

Abstract

A compact and lightweight synthetic aperture radar (SAR) that can be loaded on a miniature unmanned aerial vehicle (UAV) was recently developed. The higher the frequency is, the smaller is the antenna size and the microwave characteristics are improved. Thus, a high frequency is favorable for miniaturization and weight reduction. In this chapter, a method of obtaining a radar image through a 94-GHz frequency modulation continuous wave (FMCW) radar is proposed. In addition, a method of motion compensation is described, and the W-band SAR image after motion compensation is confirmed. This kind of SAR imaging can provide geographic information and characteristics of extreme environments, disaster scenes, and information on sites where human access is difficult.

Keywords: synthetic aperture radar (SAR), frequency modulation continuous wave (FMCW), radar, imaging, W-band, motion compensation

1. Introduction

Airborne and space-borne synthetic aperture radar (SAR) images are used in various fields of remote sensing [1]. There are various applications in using high-resolution radar images. Several imaging algorithms were developed in the laboratory, which depend on the given geometry [2–4]. SAR technology can be used to acquire images of disaster areas or other dangerous sites where direct human access is difficult. Traditional optical images have limitations, such as being weather- and environment-dependent, being too bright, or having no range information. As an alternative imager, the SAR can be loaded onto an unmanned aerial vehicle. SAR equipment was once too heavy and bulky for such an application. However, owing to recent technological improvements, radar has become smaller and more lightweight [5–7]. In particular, frequency

modulation continuous wave (FMCW) radar was developed as a chip and is lightweight, has a small size, and offers low power consumption, which has advantageous qualities for being mounted on a drone. FMCW radar can also be used at a close range. Attempts are being made to replace conventional radars with FMCW types for small and close-range systems. The higher the frequency is, the smaller is the antenna size. Thus, a high frequency is favorable for miniaturization and weight reduction [8–10]. In this chapter, FMCW radar with a center frequency of 94 GHz is used. FMCW radar is commonly employed for relatively short distances. Also, a high-range resolution can be obtained, even though it has a low sampling rate [11, 12]. The developed FMCW radar only measures real components; nevertheless, it can obtain complex data by using the Hilbert transform [13–16].

The higher frequency used in the proposed W-band SAR causes a narrower antenna beam width. Because the range is short and the width is narrow, range migration in SAR data can be ignored. In a short range, the matched filter phase for azimuth compression should change with the range. In this study, based on the range-variant azimuth chirp rate of the range Doppler algorithm (RDA), a SAR algorithm at a close range was developed and a resolution analysis of an impulse target was performed.

In the airborne SAR, the movement of the aircraft greatly affects SAR focusing. Motion compensation is important because small and slow-flying objects have less inertia and are thus more notably affected by disturbances. Therefore, to obtain decent SAR images, the motion must be compensated. Motion information is acquired by navigation sensors and used for focusing SAR images by compensating them. The quality of the reconstructed image is very sensitive to the geometry determination accuracy. This factor has led to the development of autofocusing techniques.

Several methods for autofocusing exist, such as entropy minimization [17], an FMCW analytic method [18], contrast optimization [19] in ISAR, phase gradient autofocusing (PGA) [20, 21], and prominent point processing (PPP) [22] in SAR. These methods consist of range alignment and phase compensation. Moreover, they are applicable to circular synthetic aperture radar (CSAR) with wideband SAR [23]. A SAR or ISAR autofocusing method using a prominent target was proposed [22, 24]. However, this method requires a prominent target, and it is difficult to find an ideal point target. Nonetheless, this method is faster than contrast maximization [19] or entropy minimization [17, 25]. The algorithm based on contrast maximization is slow because of a high computing cost. It is difficult to apply these autofocusing methods because focusing cannot be performed when the motion is large. Therefore, navigation sensors that can provide position and velocity information, such as GPS and IMU, are needed to compensate for motion.

The purpose of the proposed algorithm is to implement a video SAR with a high frame rate through fast signal processing. It is possible to obtain SAR images, such as videos, using W-band. The video SAR helps intuitively recognize moving objects. Recent research has contributed to the increase in the real-time frame rate [26–28]. Therefore, a simple SAR focusing algorithm and motion compensation should be implemented.

This chapter describes a method of compensating the motion caused by disturbance of the W-band SAR platform. Focusing from the SAR received data with arbitrary movement is

evaluated in the laboratory, where arbitrary movement can be applied by using the motor controller. As the wavelength becomes short, the motion compensation of the aircraft should become more precise. Therefore, precise IMU and GPS navigation sensors are required. The motion obtained from the sensors must be compensated to obtain the SAR image.

An experiment was conducted in which it was assumed that accurate position information is obtained by using the motor controller. In the experiment, a 94-GHz FMCW radar developed by Yonsei University using an FPGA was used. Section 2 describes the radar architecture. Section 3 presents the proposed method for W-band SAR imaging at a close range. Section 4 describes the process of measuring SAR in well-known motions and compensating for the movements in an anechoic chamber. Section 5 provides a summary.

2. W-band radar architecture

The 94-GHz radar consists of three major parts: a transceiver, power board, and processing board. The transceiver generates the waveform, up-converts the signal to a radio frequency (RF), and radiates the signal. The power board provides power to the transceiver. The processing board samples the beat signal and transmits the data. A functional diagram of the modules is presented in **Figure 1**.

2.1. Transceiver

As shown in **Figure 2**, the transceiver consists of three parts: an antenna, front-end module, and phase-locked-loop (PLL) board. The antenna is a gold-plated brass horn antenna with linear polarization. It has 25-dBi gain at 94-GHz frequency, and an approximately 10-degree half-power beam width. The antenna is connected to the front-end module with a rectangular

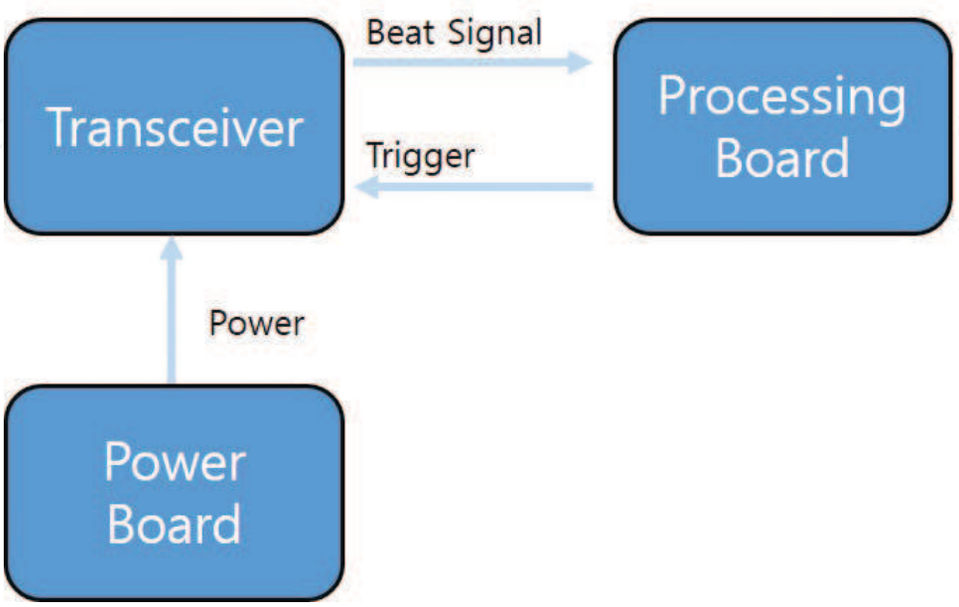

Figure 1. Functional diagram of developed radar.

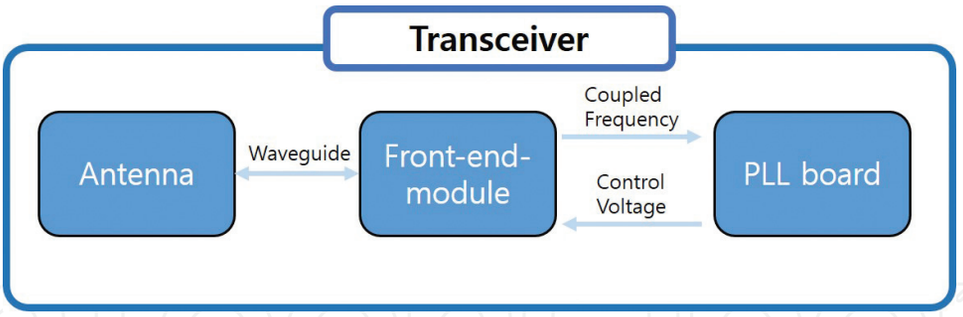

Figure 2. Functional diagram of a transceiver.

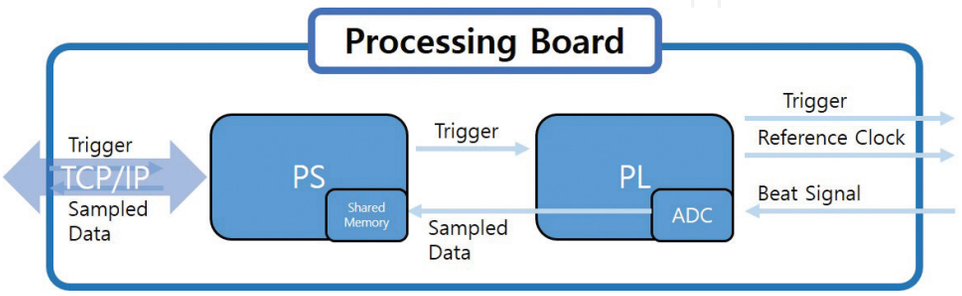

Figure 3. Functional diagram of the processing board.

waveguide interface [13]. The front-end module consists of a voltage-controlled oscillator (VCO), power amplifier, frequency multiplier, bypass mixer, and multistage low-noise amplifier. Its output center frequency is 94 GHz with a sweep bandwidth of 1.4 GHz, which is adequate for providing a resolution up to 0.12 m. The RF output power is 1.5–2 mW. Its receiver low-noise amplifier (LNA) gain can be selected from 23 to 46 dB. To synchronize the front-end module with the processing board, a PLL board is used. The PLL board synchronizes the oscillation from the front-end module with the processing board's clock. It also provides the voltage sweep required to sweep the VCO output frequency.

2.2. Processing board

The processing board utilizes the Xilinx Zynq-7000 chip for analog-to-digital conversion (ADC), synchronization with the PLL board, triggering the PLL board, and data transmission. The chip is divided into two parts: programmable logic (PL) and a processor (PS) [14]. Its functional diagram is presented in **Figure 3**. The processing board's main tasks are to provide the trigger and clock for the PLL, sample the beat signal from the transceiver, and send the raw data via TCP/IP. The beat signal from the front-end module is sampled by an analog-to-digital converter inside the PL at a sampling rate of 940 KHz. When the PL receives the radar command from the PS, the latter writes the sampled data to the shared memory. The PS then reads the sampled data from the shared memory and transmits the raw data via TCP/IP [29].

Figure 4 shows the FMCW radar block diagram. **Figure 5** shows the radar module, processing board, power board, PLL, front-end module, and antenna.

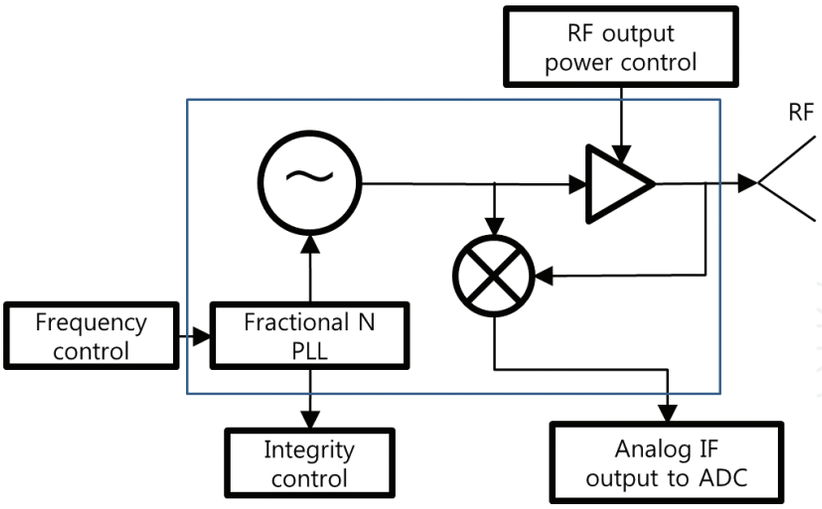

Figure 4. Flow diagram of FMCW radar.

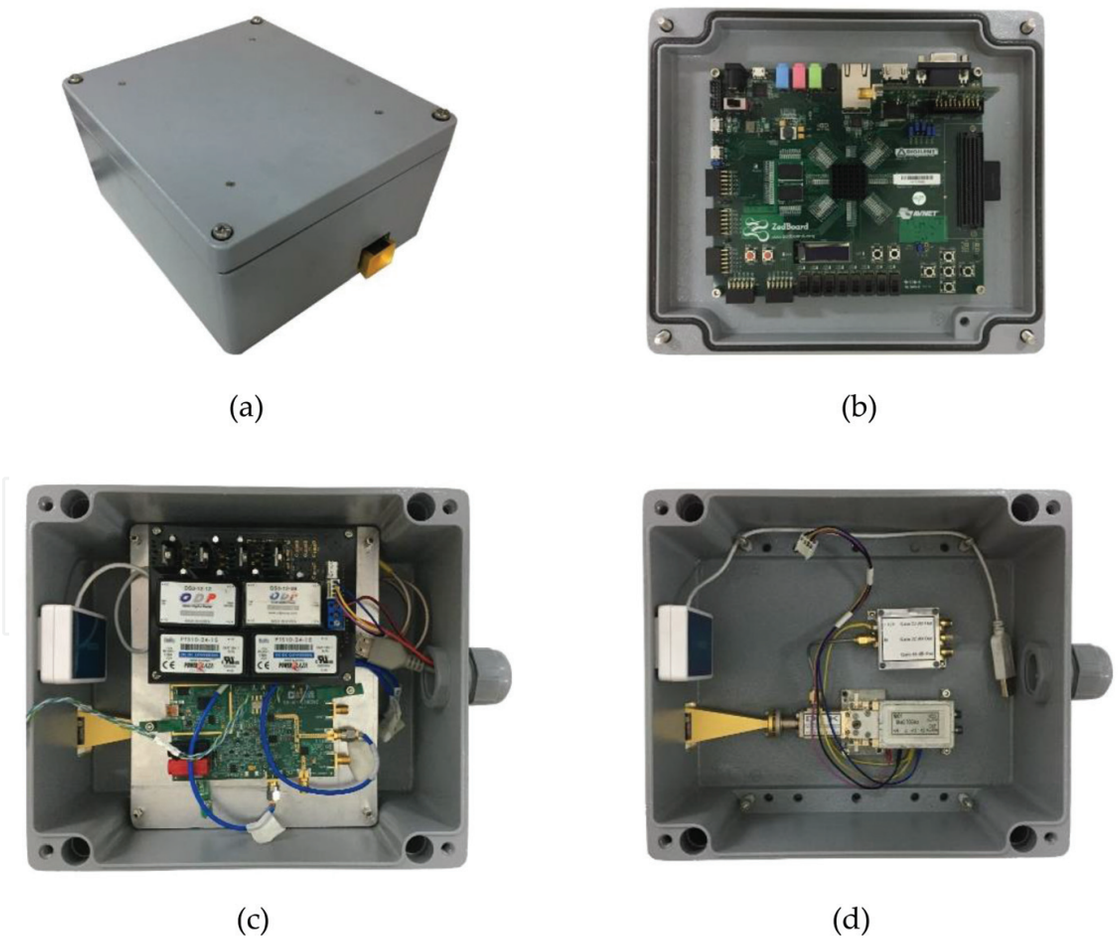

Figure 5. Developed 94-GHz radar: (a) radar module, (b) FPGA signal-processing board, (c) PLL and power board, and (d) front-end module and antenna.

2.3. Power board

The power board consists of four power converters and four regulators. It was designed to provide the transceiver with the required power for each module. After providing the transceiver with its appropriate voltage level, the power consumption of the radar is approximately 10 W.

2.4. FMCW radar performance

An FMCW [30–34] is a signal whose frequency is continuously modulated. The transmitted signal can be represented by.

$$s(t) = e^{2\pi j\left(f_0 t + \frac{1}{2}kt^2\right)} \tag{1}$$

where f_0 is the carrier frequency and k is the chirp rate. The echo signal is mixed with the transmitted signal to from the received signal. The received signal from a single target can be represented as.

$$s_r(t) = e^{2\pi j\left(f_0 t + \frac{1}{2}kt^2\right)} \cdot ae^{2\pi j\left(f_0 (t-\tau) + \frac{1}{2}k(t-\tau)^2\right)} = ae^{2\pi j\left(f_0 \tau + \frac{1}{2}k\tau^2\right)} e^{-2\pi jkt\tau} = ae^{j\varphi} e^{-2\pi jkt\tau} \tag{2}$$

where ϕ is the constant phase. The received signal for a single target is sinusoidal and its frequency depends on the target range. The transmitted signal of the FMCW radar is modulated with respect to time, and the received signal from the impulse target is a beat frequency, f_b, which is the difference between the transmit frequency and the received frequency. The beat frequency is proportional to the range of the target and is represented as.

$$f_b = k\tau = \frac{BW}{t_r}\frac{2R}{c} \tag{3}$$

The FMCW radar repeatedly and continuously transmits the waveform given in Eq. (1). The waveform is classified into saw-tooth and triangular waveforms according to the repeated form. The time it requires to sweep the frequency is called the ramp time, t_r. Then, the bandwidth of the FMCW is defined as.

$$BW = kt_r \tag{4}$$

The radar used in the experiment was FMCW radar with a center frequency of 94 GHz. The radar transmitted the linear frequency modulation (LFM) signal through the antenna, and it sampled the echo signal mixed with the transmitted signal. The chirp of the LFM signal used was an up-ramp saw-tooth waveform. The chirp rate, k, was 1400 MHz/ms and the ramp (sweep) time was 1 ms. The sampling rate was 940 KHz. The bandwidth was 1.4 GHz, and the signal could be sampled 940 times in a single period. According to Eq. (3), the range can be represented by the function of the beat frequency as.

$$R = \frac{cf_b}{2k} \tag{5}$$

The received signal is converted to a range profile by inverse fast Fourier transform (IFFT). The range profile of a single target is obtained using Eq. (3), which is shown as.

$$S_r(f,R) = ae^{j\varphi}\int_{-\infty}^{\infty} w(t_r)e^{-2\pi jkt\tau}\cdot e^{2\pi jft}dt = ae^{j\varphi}\mathrm{sinc}(tf-k\tau) \tag{6}$$

where the window, $w(t_r)$, serves only to take one period of the signal, and sinc(x) is a normalized sinc function. In the case of saw-tooth FMCW, the beat frequency is obtained by performing the FFT on the range profile.

Taking the displacement on both sides of Eq. (5) gives Eq. (7). The range resolution is determined by a sinc function of the range profile.

$$\Delta R = \frac{c\Delta f}{2k} = \frac{ct_r\Delta f}{2BW} = \frac{cNt_s\Delta f}{2BW} = \frac{c}{2BW} \tag{7}$$

where t_s is the sampling interval, 1.06 μs, and N is the number of samples in an echo, 940. The beat frequency resolution is 1.49 MHz. The theoretical properties of the point target response for FMCW radar is a 1.4-Ghz bandwidth or a resolution of approximately 0.093 m. If the bandwidth increases, a profile with a high-range resolution can be obtained. The FMCW radar does not require a sampling rate above the bandwidth to avoid degrading resolution.

$$\Delta R_0 = \frac{r_r f_s}{N_{IFFT}}\frac{c}{2BW} \tag{8}$$

The range resolution depends on zero padding. However, according to the Fourier transform properties, Nt_s is equal to $1/\Delta f$. The range cell thus had a spacing of 0.15 m. Therefore, 8912 samples were used for FFT after padding 7912 zeros. The range cell spacing after zero padding was 0.015 m. The range cell spacing after zero padding was sufficiently smaller than the range resolution.

There is no minimum range limit in FMCW radar. However, the maximum range is limited by two parameters. For one, the maximum range is limited by the sampling rate. This is because the beat frequency is determined by the Nyquist frequency, which is equal to half the sampling rate. Another criterion is the range ambiguity. For FMCW, when the delay time becomes half of the ramp time, the resolution doubles. Depending on the conditions, this value may vary; however, in Eq. (9), 10% was chosen [35]. Usually, in FMCW radar, the ramp time is adequately long and the target signal exists only within the radar range of interest. Thus, the maximum range is determined by the sampling rate.

$$R_{\max} = \begin{cases} \dfrac{ct_r f_{\max}}{2BW} = \dfrac{ct_s f_s}{4BW} = \dfrac{cN}{4BW} & \text{for the Nyquist criterion} \\ 0.1\dfrac{ct_r}{2} & \text{for the range ambiguity} \end{cases} \tag{9}$$

Because the sampling rate is high, the distance information of farther targets can be obtained if the beat frequency resolution increases. The maximum range criterions are sufficiently longer than the length of the chamber. Therefore, aliasing will not occur. The maximum range of

FMCW radar is 15,000 m for the ambiguous range and 477 m for the Nyquist criterion. The chamber subjected to the experiment had a length of approximately 7 m.

The radar performance was analyzed using a trihedral corner reflector target. The experimental settings are shown in **Figure 6**. The target and the radar were placed inside an anechoic chamber with a target distance of 2.8 m.

As shown in **Figure 4**, the radar samples the echo signal multiplied by the transmitted signal. The sampled signal is the de-ramped signal of the echo, where the frequency components are sampled. Therefore, when conducting an inverse Fourier transformation (IFT), the symmetric value of the time or range domain can be obtained. Because only the in-phase component can be obtained, only the real number or in-phase components of Eq. (2) can be obtained as the received data. Through the Hilbert transformation, a quadratic component (imaginary part) can be generated. The Hilbert transformation is a method for generating a signal that has the same magnitude but is orthogonal to the original signal [15]. As shown in Eq. (10), the Hilbert transformation is used to obtain an in- phase/quadratic (I/Q) signal. When performing the IFT with this method, the phase information can be obtained, and the symmetrical information, which can be generated as a mistaken IFT, can be prevented.

$$s_h(t,n) = s(t,n) + jH_h(s(t,n)) \tag{10a}$$

$$S_r(f,n) = IFFT[s_h(t,n)]_t \tag{10b}$$

The experimental results from a point target are shown in **Figure 7**. Theoretically calculated side-lobe level, resolution and experimental results are almost identical.

The side-lobe level, null-to-null resolution, and 3-dB resolution of the impulse target were analyzed [36]. The measured resolution of the FMCW radar, as shown in **Figure 7**, is expressed in **Table 1**, which describes the resolution in the range direction. It can be observed that the theoretical resolution of 0.09 m and the measured resolution (3 dB) are very close.

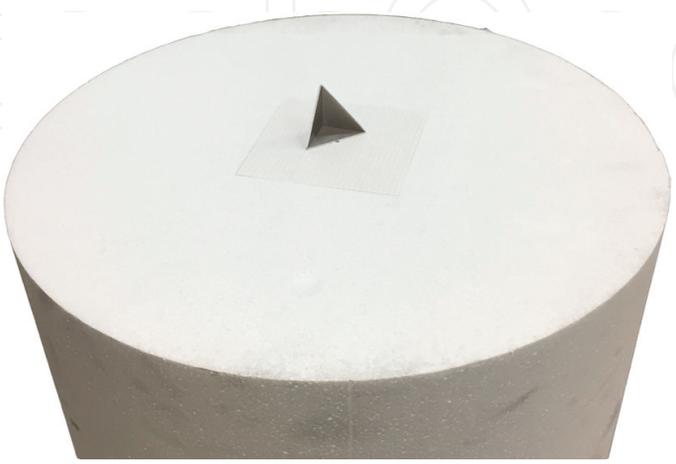

Figure 6. Experiment settings for the impulse target.

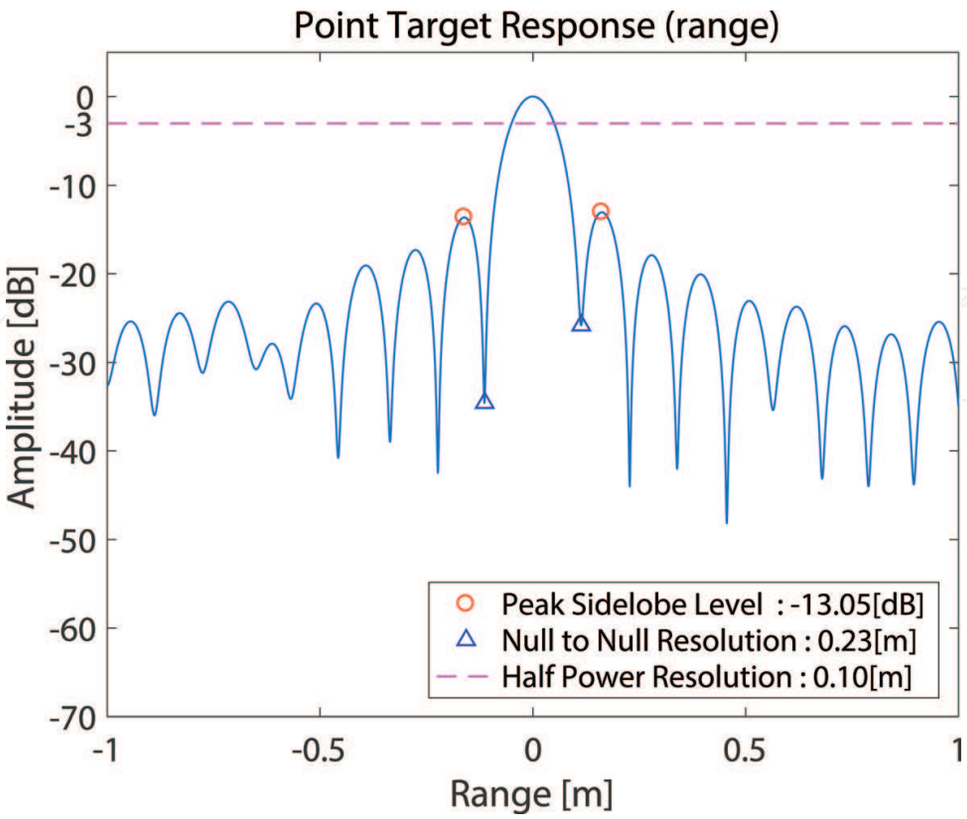

Figure 7. Point target response in the range direction.

Peak side-lobe level	**−13.05 dB**
Null-to-null resolution	0.23 m
3-dB resolution	0.10 m

Table 1. Measured resolution of the range direction.

3. SAR image formation

3.1. Experimental settings

SAR experiments were conducted using the FMCW radar described in Section 2. An experimental diagram is shown in **Figure 8**. The experiment was conducted inside an anechoic chamber with a maximum range of 7 m. The broadside-facing radar was placed on a rail moving in a cross-range direction to the target. The total synthetic length was 2 m and the target was in a range of 2.8 m. The target was a trihedral corner reflector. **Figure 9** depicts the experimental settings, which assumed a non-squint radar geometry and that the antenna was oriented perpendicular to the track direction during motion. The rail motion was controlled by a motor. As shown in **Figure 8**, the radar platform moved along the rail. Because its flying

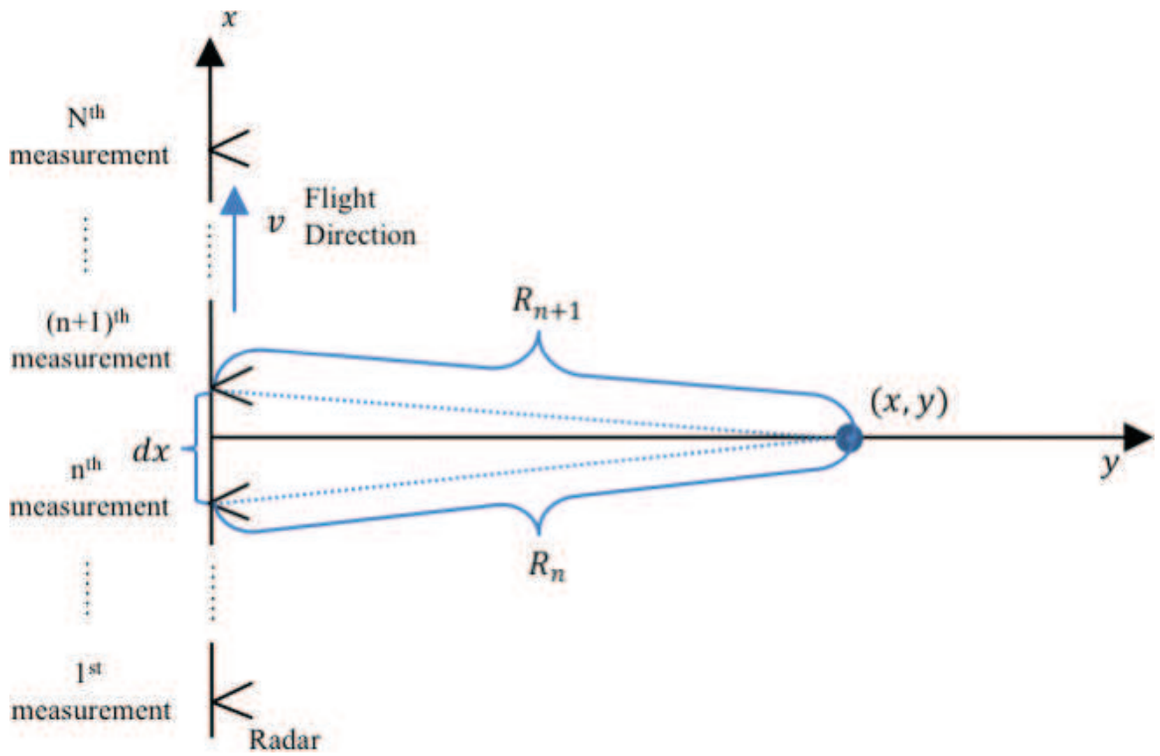

Figure 8. Diagram of SAR experiment settings.

speed was low, the interval on the rail was set to 0.001 m. The total number of measurements was 2001.

3.2. Range profile

The transmitted signal was scattered by the target. The nth-received signal from the impulse target after IFFT was $S_r(n)$ and is written as Eq. (11). As shown in Eq. (2), the phase delayed received signal can be represented. Herein, R_i refers to the distance between the antenna and the target, and a_i refers to the ith-scattering coefficient and antenna pattern with respect to the observation angle. In addition, p(f) refers to the impulse response without a delay and λ refers to the signal wavelength. The range profiles of all 2001 measurements are shown in **Figure 11**.

$$S_r(f, n, R_i; x_i, y_i) = \sum_{i=1}^{N} a_i(n)p(f)e^{-4\pi j R_i/\lambda} = \sum_{i=1}^{N} a_i(n)p(f)e^{-4\pi j\sqrt{x_i^2+y_i^2}/\lambda} \tag{11}$$

A single range profile at the center of the synthetic aperture is shown in **Figure 10**. The target signal is visible at a range of 2.8 m. Such range profiles can be stacked with regard to the antenna position to form a two-dimensional range profile, which is shown in **Figure 11**. As the figure illustrates, a frequency of 94 GHz and a narrow beam width of approximately 10° were used. The target with a relatively short distance was measured.

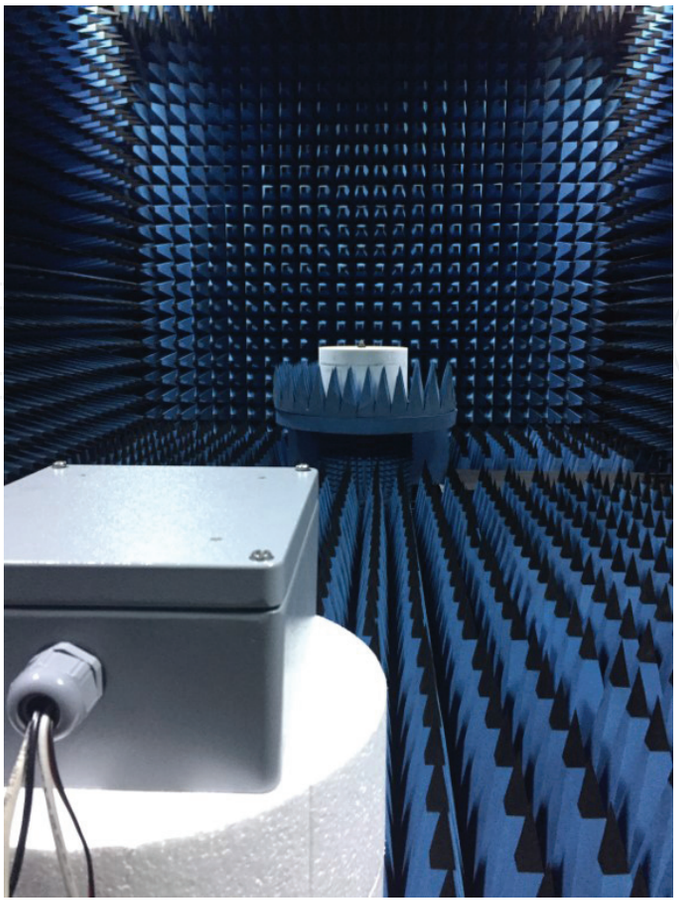

Figure 9. Configuration of experimental settings.

$$\delta R = \frac{R}{\cos\theta/2} - R = \Delta R \tag{12}$$

The difference between the bore sight range and the antenna of 3-dB edge sight range can be represented as Eq. (12). The range cell migration can be neglected because the difference is sufficiently less than the range resolution.

3.3. Azimuth compression

The target signal phase changes with respect to the antenna position. From **Figure 8**, the phase history of the point target located at x_0 and y_0 can be derived as Eq. (13).

$$\theta\left(n, R_0 = \sqrt{x_0^2 + y_0^2}\right) = \frac{4\pi}{\lambda}\sqrt{(x_0 + ndx)^2 + y_0^2} \approx \frac{4\pi}{\lambda}\left[\frac{x_0^2}{2y_0} + \frac{(ndx)^2}{2y_0} + \frac{x_0}{y_0}ndx + y_0\right] \tag{13}$$

The azimuth compression can be performed by using Eq. (13) to create a matched filter along the cross-range direction. Since the curvature of phase in Eq. (12) varies with range, a

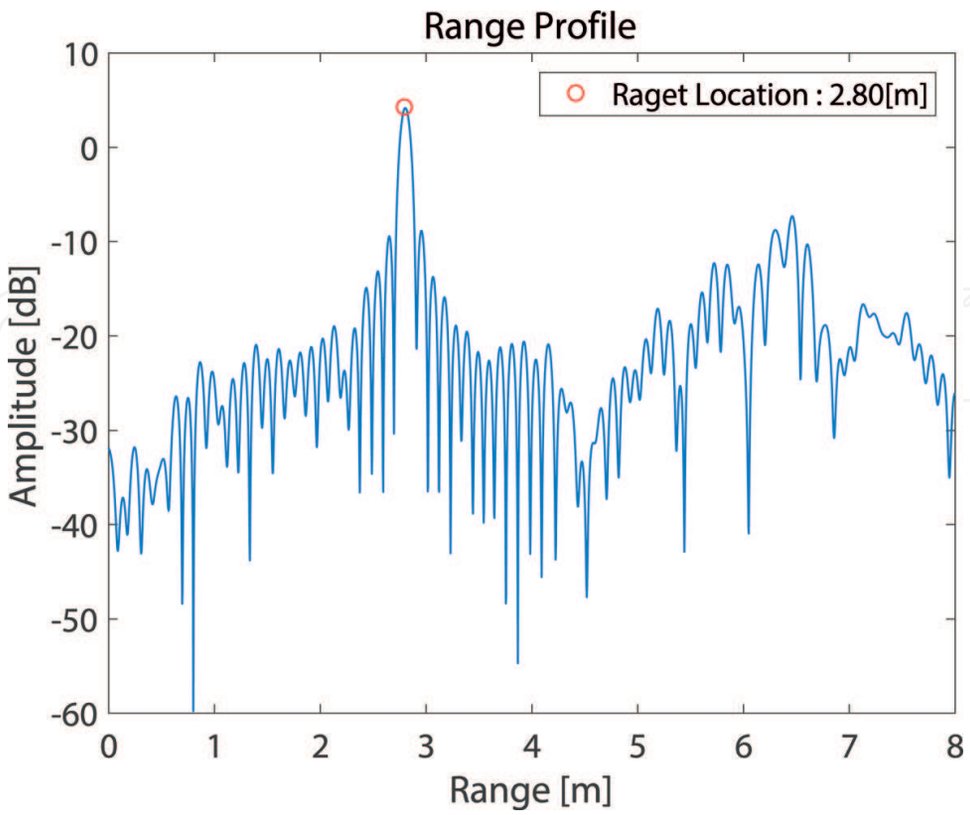

Figure 10. Range profile of the impulse target.

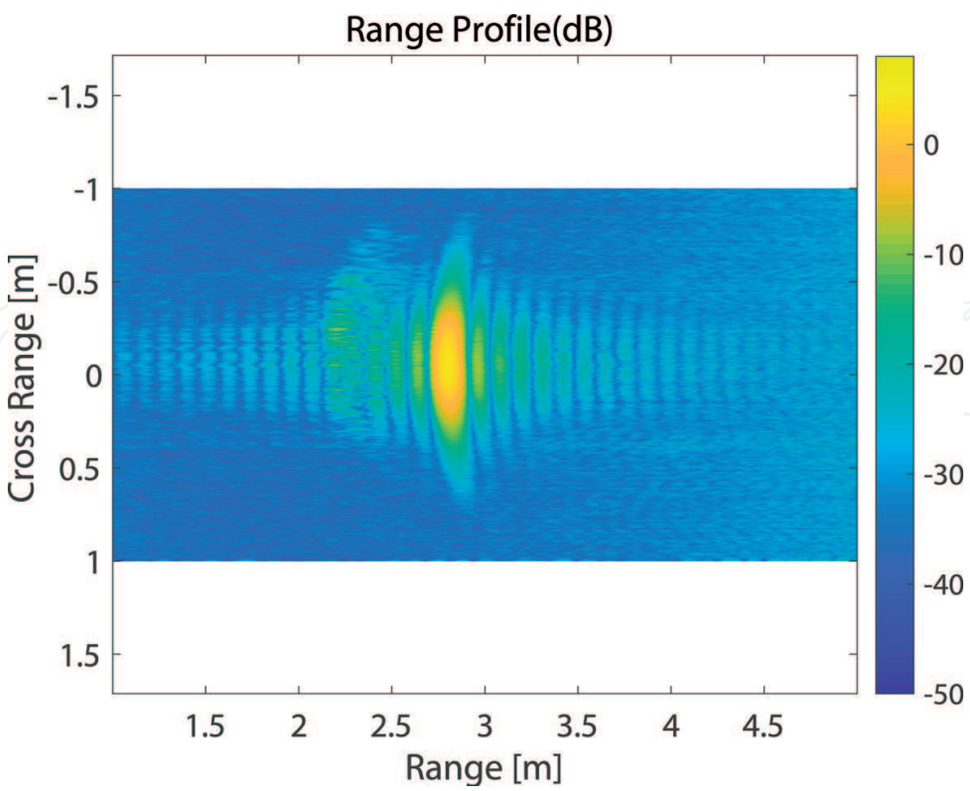

Figure 11. Measured range profile in two dimensions.

different azimuth-matched filter must vary with the range. **Figure 13** shows the azimuth compression filter.

$$\begin{aligned} S_{SAR}(f,n) &= IFFT\left[FFT[S_r(f,n)]_n * FFT[S_{MF}(y,n)]_n^*\right] \\ &= IFFT\left[FFT[S_r(f,n)]_n * FFT\left[e^{j\theta(y,n)}\right]_n^*\right] \end{aligned} \tag{14}$$

The SAR image is obtained through the azimuth compression, as shown in Eq. (13). The process of obtaining the SAR image using the FMCW radar is shown in the flow chart in **Figure 12**.

After applying the azimuth compression filter (**Figure 13**) to the two-dimensional range profile (**Figure 11**), the azimuth-compressed SAR image of the impulse target is obtained, as shown in **Figures 14** and **15**.

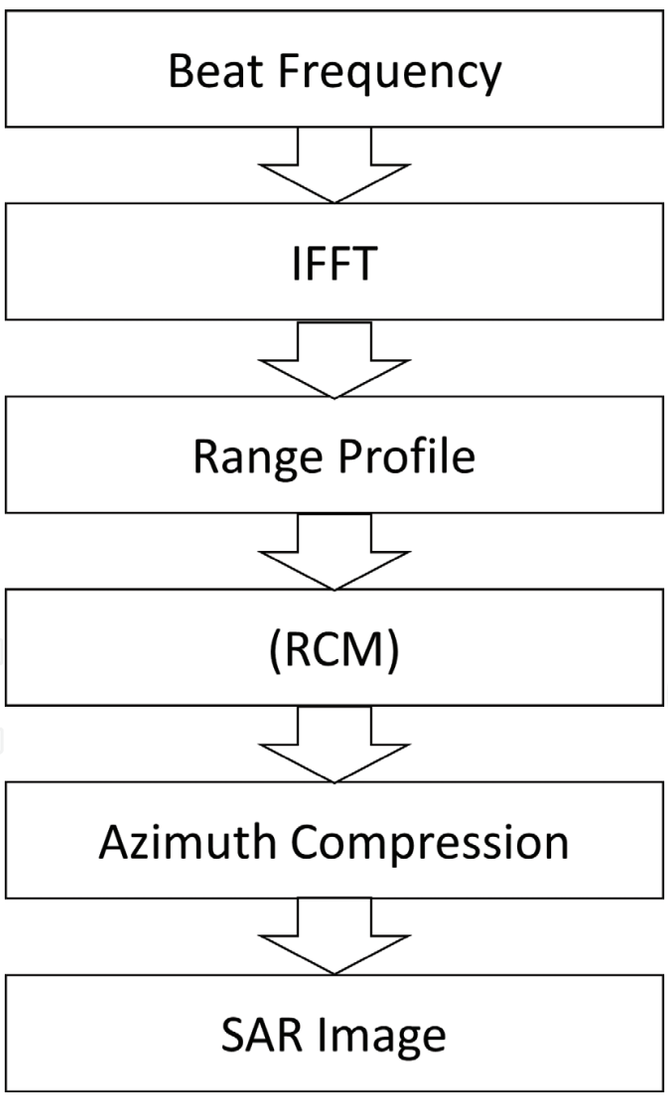

Figure 12. Flow diagram of SAR imaging. In the W-band, RCM does not have to be used depending on the range and the antenna beam width.

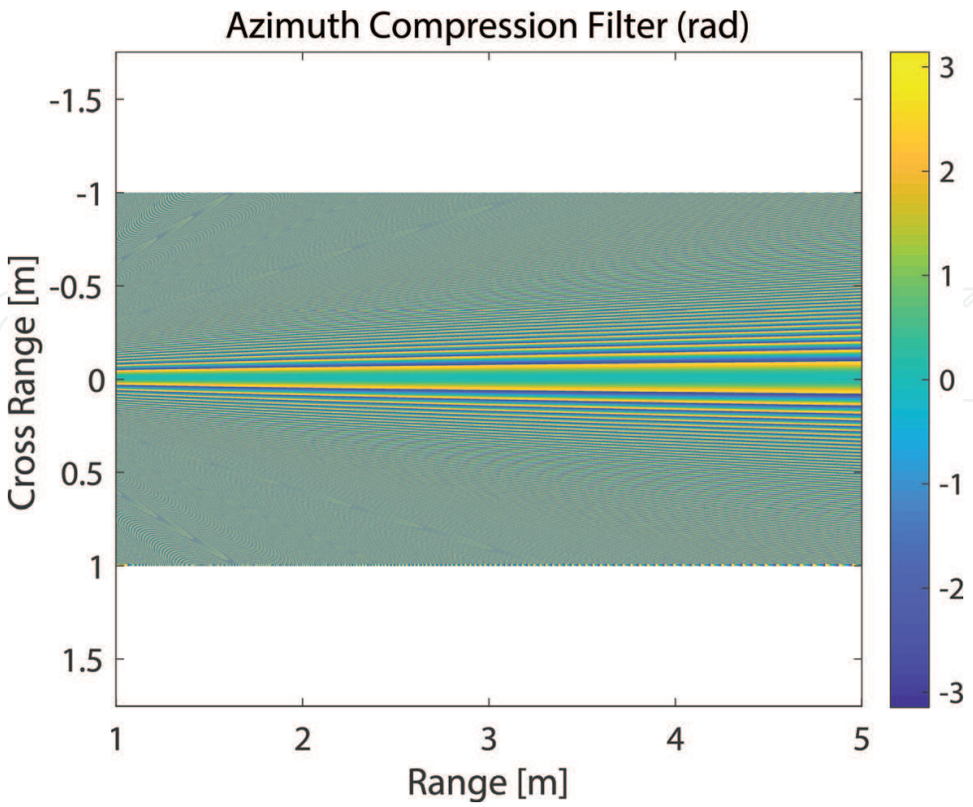

Figure 13. Azimuth compression filter.

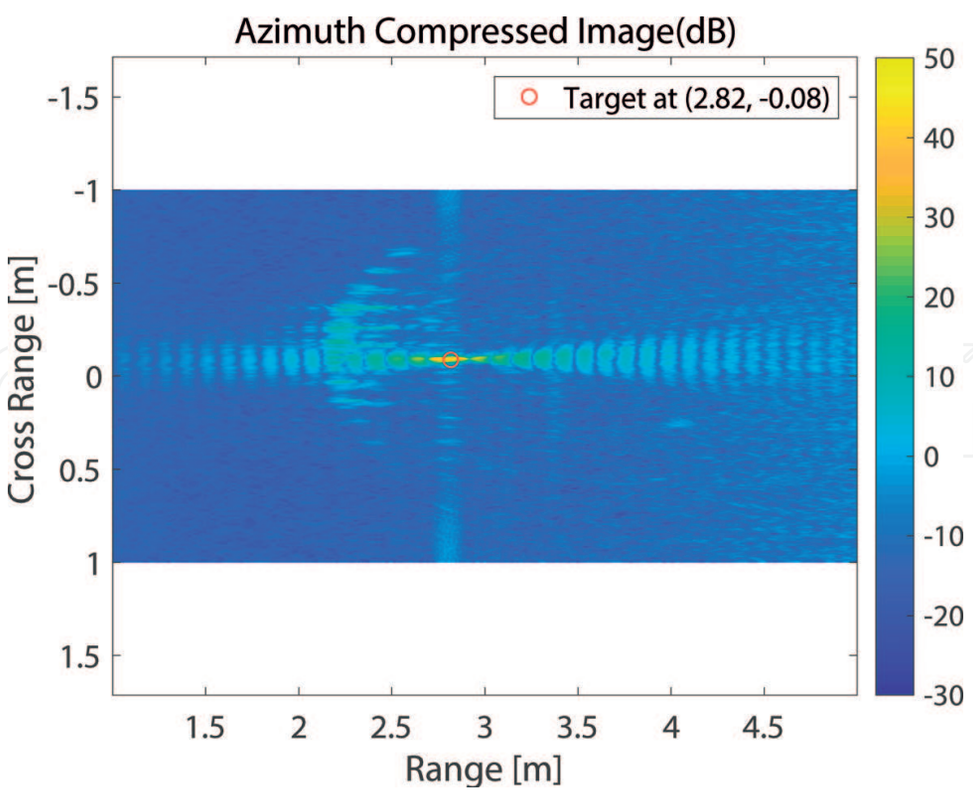

Figure 14. Azimuth-compressed SAR image.

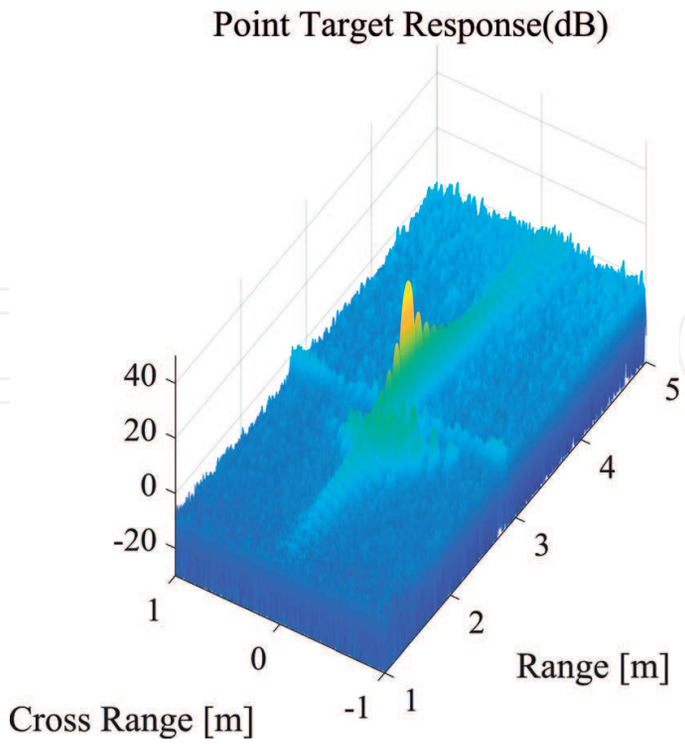

Figure 15. Azimuth-compressed SAR image shown in three dimensions.

The range profile in the SAR image can be represented in **Figures 16** and **17**. The range resolution of the SAR image is lower than the impulse range response shown in **Figure 7**. This degradation is estimated to be due to azimuth compression and may be improved via a precise range cell migration.

3.4. Cross-range profile

The cross-range profile at a target range can be obtained by taking a column from the SAR image. This profile with the target location is shown in **Figure 18**.

A detailed analysis of the point target is shown in **Figure 19**, including the side-lobe level and resolution. The theoretical null-to-null cross-range resolution of the SAR image can be calculated using Eq. (14) [37].

$$\delta y_{nn} = \frac{\lambda}{2\theta} = 0.0183 \text{ m} \tag{15}$$

Because the target range is small, the synthetic length is governed not by the antenna position but by the antenna beam width. The 3-dB beam width of the antenna, that is, 10°, was used for the calculation. **Table 2** outlines the resolution in the cross-range direction. The cross-range null-to-null resolution is 0.0183 m, and the cross-range half-power resolution (3 dB) is 0.0076 m, as measured by the SAR experiment using the impulse target, as shown in **Figure 19**. The experimental null-to-null resolution matches the theoretical expectation of 0.0183 m from Eq. (15).

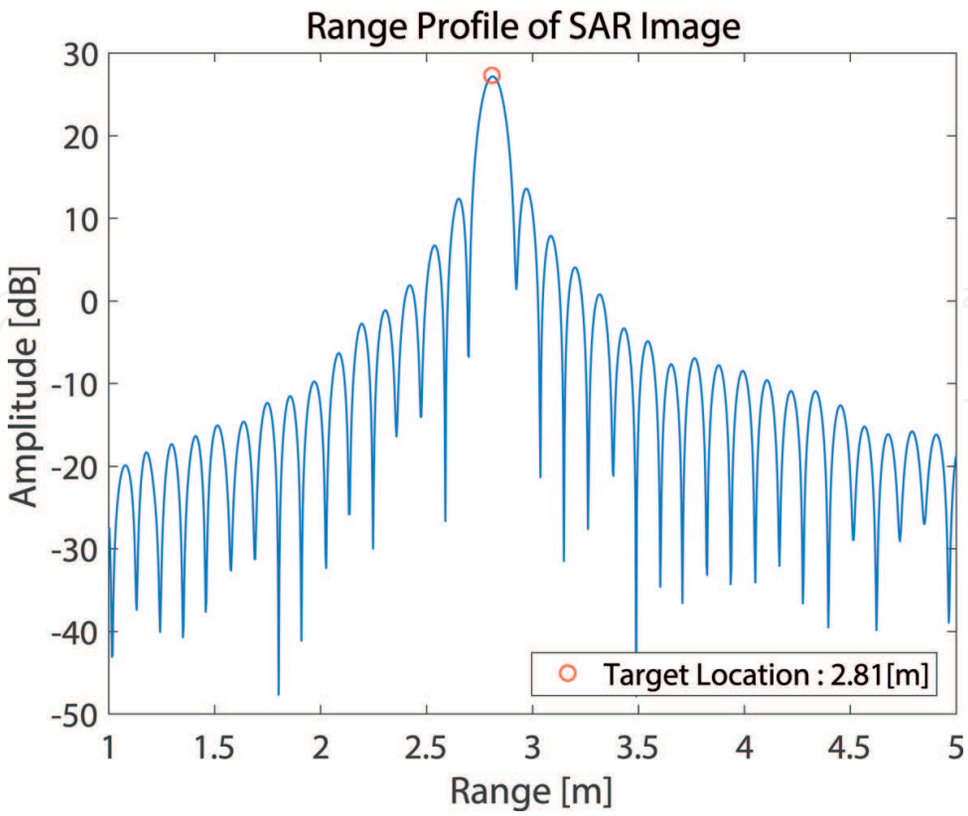

Figure 16. Range profile in SAR image.

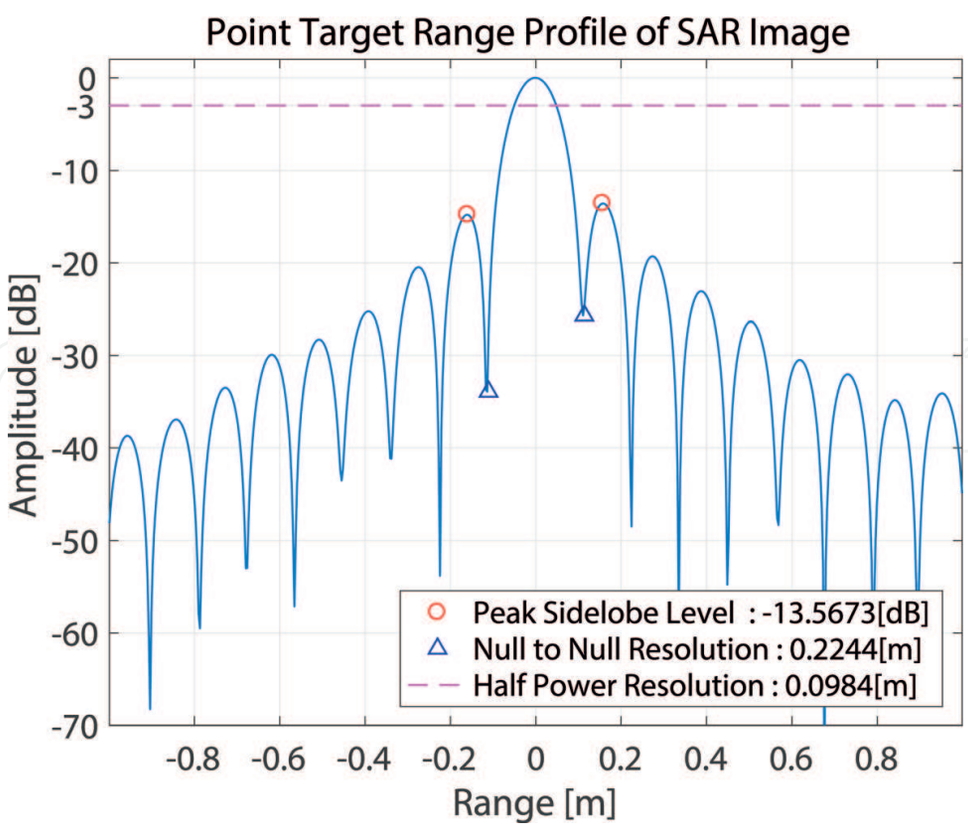

Figure 17. Point target profile in SAR image.

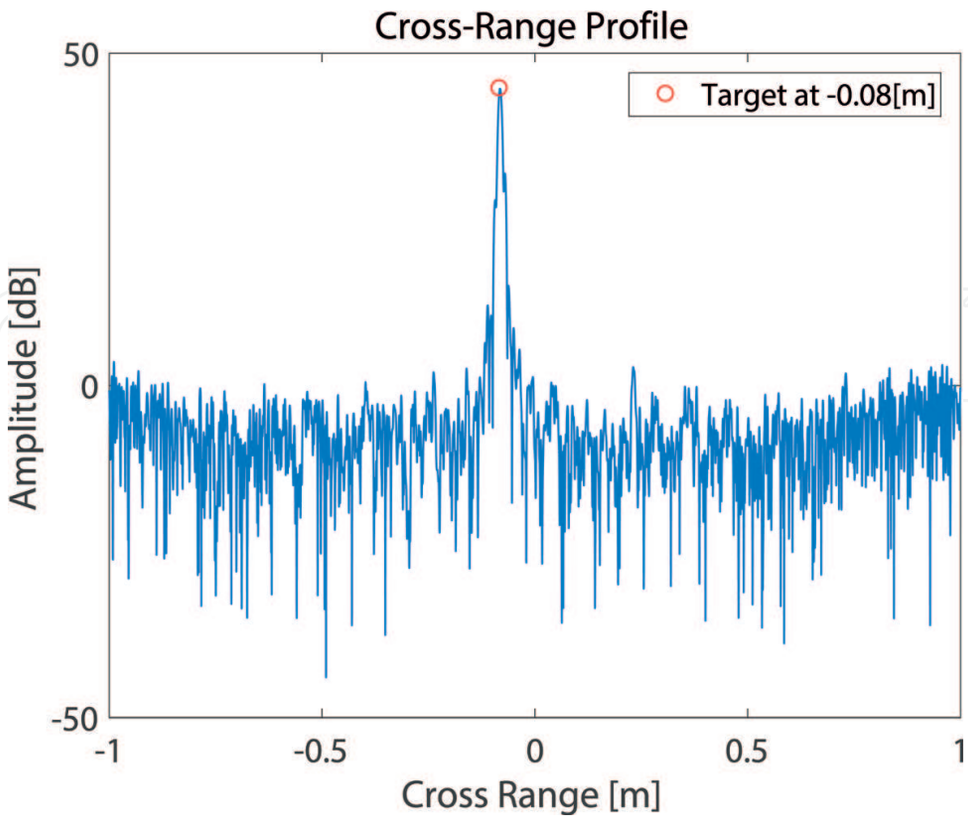

Figure 18. Cross-range profile of the impulse target.

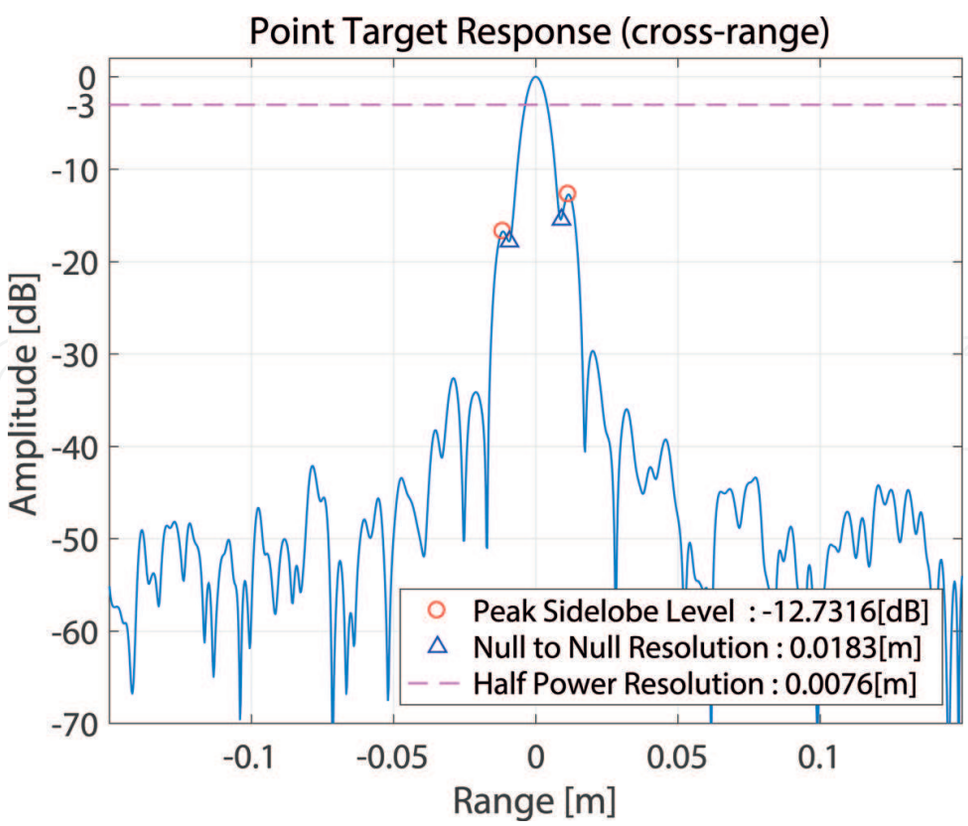

Figure 19. Detailed analysis on the cross-range profile of the impulse target.

Peak side-lobe level	**−12.73 dB**
Null-to-null resolution	0.0183 m
3 dB resolution	0.0076 m

Table 2. Measured cross-range resolution of SAR.

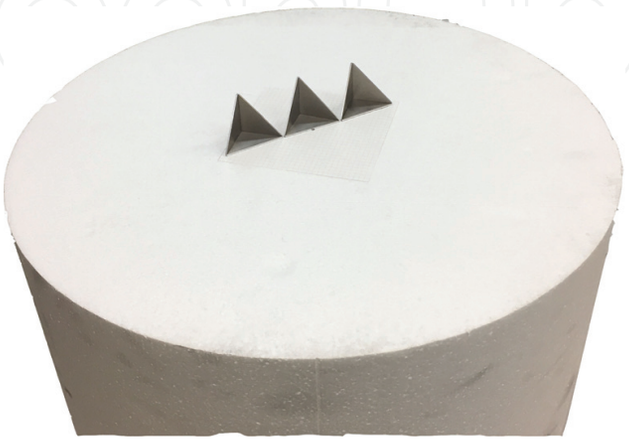

Figure 20. Experimental settings of multiple targets.

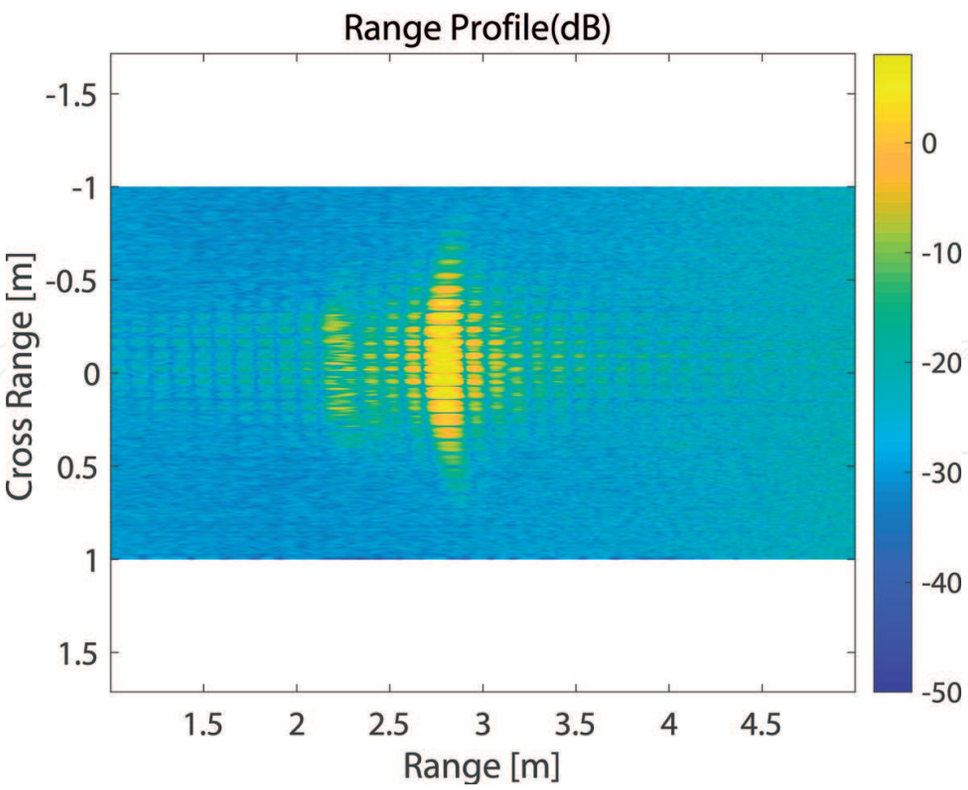

Figure 21. Measured range profile for three corner reflectors.

http://dx.doi.org/10.5772/intechopen.74692

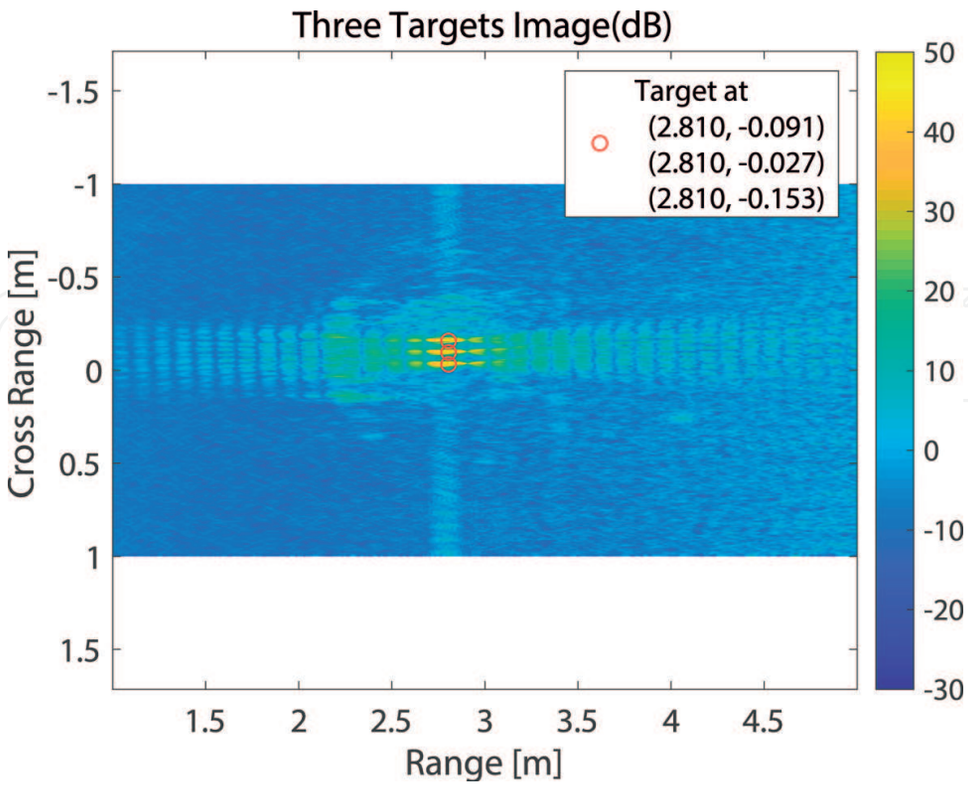

Figure 22. SAR image of multiple targets.

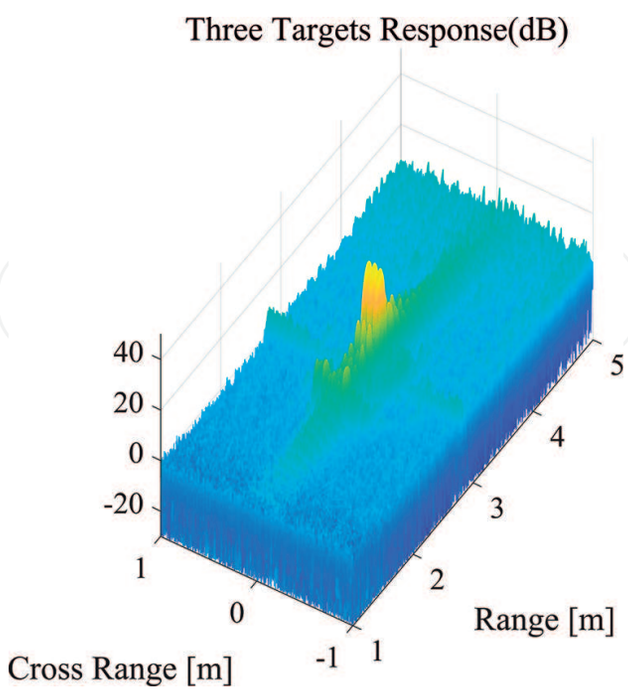

Figure 23. Azimuth-compressed SAR image of the multiple targets shown in three dimensions.

3.5. Multiple targets

An experiment was conducted in which three corner reflectors 0.06 m apart from each other were placed at a range of 2.8 m. The target settings are shown in **Figure 20**.

By using the same processing in Section 3.3, a SAR image of multiple targets was obtained. The range profile for the three corner reflectors is shown in **Figure 21**. Using the azimuth compression method in Section 3.3, the SAR images were obtained. The SAR image is shown in **Figure 22**, where its magnitude is in the decibel scale. The three-dimensional SAR image is shown in **Figure 23**. The positions of the corner reflectors are approximately 0.06 m apart in the cross-range direction. The targets are located close to the cross-range direction; nevertheless, they are clearly distinguishable. Any arbitrary object can acquire SAR images using the above SAR-focusing method. This SAR-imaging method is very simple; however, it is a powerful method for acquiring real-time SAR images.

4. Motion compensation

In the case of the airborne SAR, movement due to external disturbances can easily occur. Navigation devices, such as GPS and IMU, can record such motion. To focus the SAR image, the motion must be compensated. Motion compensation has been studied for decades, as described in [38–41]. Since W-band has a short wavelength, accurate motion compensation is

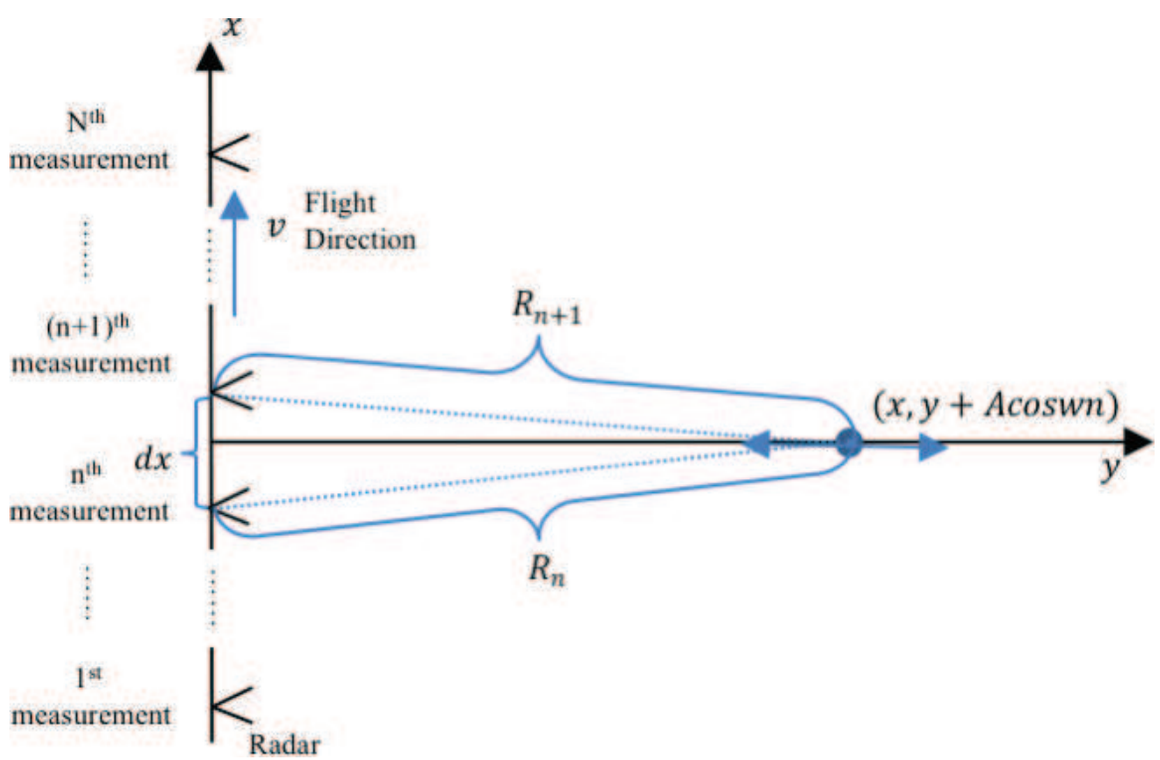

Figure 24. SAR geometry with motion.

required. A method of applying and verifying the motion compensation to the simple SAR focusing shown in Section 3.3 is herein introduced.

To verify the motion compensation algorithm, the target was measured by adding motion to the SAR technique, as shown in **Figure 24**. Similar to the experiments in Section 3, the radar moved in the cross-range direction. However, in this case, the target also moved in the range direction. In practical situations, the radar has a movement in the range direction with stationary targets.

The above conditions are that the target is moving and general conditions move the platform, which are equivalent. Thus, for experimental convenience, the experiment in which the target moved was conducted. The target had a sinusoidal motion with an amplitude of 0.4 m, as shown in **Figure 25**. The amplitude of this motion was several times larger than both the range cell and the wavelength. Therefore, it was necessary to compensate for the range bin and phase in the range profile of the received signal.

The other conditions were the same as those in the experiments noted in Section 3. The SAR image acquisition method is now discussed with compensation for this motion. The motion of azimuth direction is known to be compensated by interpolation [39, 42, 43]. Thus, it is not considered in this experiment. The motion (or acceleration) in azimuth direction can be compensated by equal-spacing azimuth sampling using interpolation. Also, the interpolation can also be used to increase the sample in azimuth direction at a high velocity of the platform.

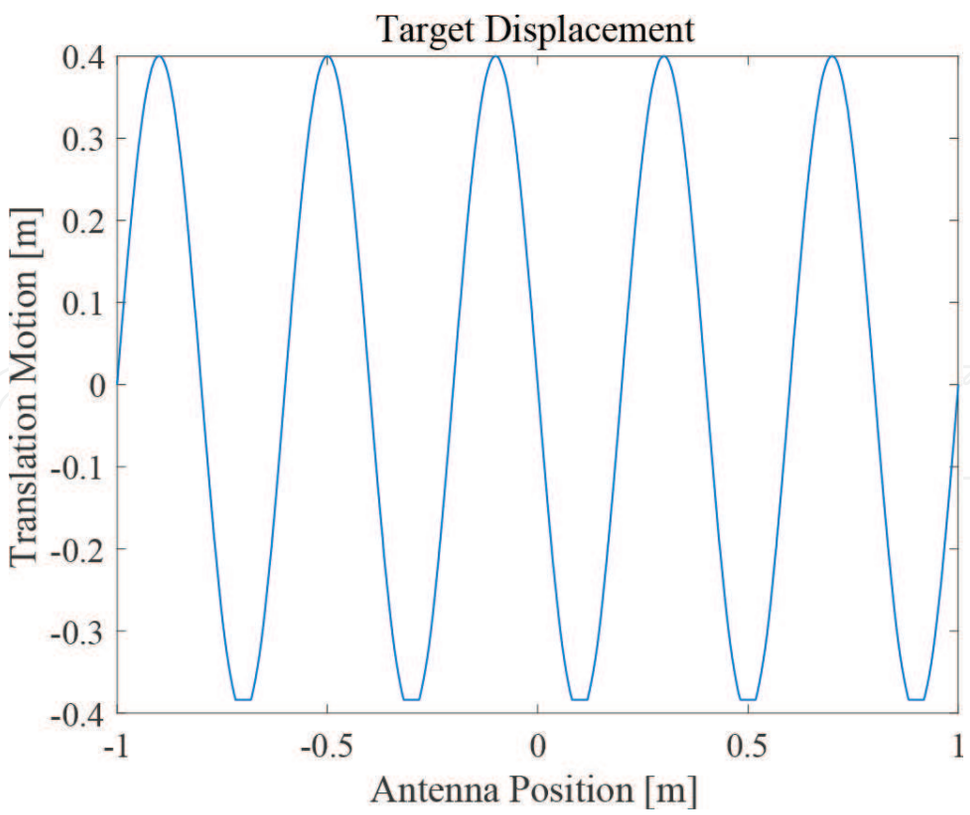

Figure 25. Movement applied to the target in the range direction.

4.1. Range bin alignment

The range profile of the impulse target located at 4.3 m and obtained under the mentioned sinusoidal motion is shown in **Figure 26**. In the figure, it can be observed that the locus of the scatterer moves in a sinusoidal direction.

The phase, including the motion in the azimuth direction, can be expressed as Eq. (16).

$$\begin{aligned}\theta'\left(n, R_0 = \sqrt{x_0^2 + y_0^2}\right) &= \frac{4\pi}{\lambda}\sqrt{(x_0 + ndx)^2 + \left(y_0 + d(n)\right)^2} \\ &\simeq \frac{4\pi}{\lambda}\left[\frac{x^2}{2y_0} + \frac{(ndx)^2}{2y_0} + \frac{x_0}{y_0}ndx + y_0 + Y_{des} + \frac{Y_{des}(n)^2}{2y_0}\right] \\ &\simeq \frac{4\pi}{\lambda}Y_{des} + \theta(n, y_0)\end{aligned} \tag{16}$$

The quadrature term of the phase in Eq. (12) and motion can be approximately represented as linear combinations. Therefore, the motion can be compensated independently of the azimuth compression.

For azimuth compression, the range bin should be aligned in the received signal (before IFFT). In the frequency domain, the delay function is represented by the phase shift. Accordingly, the received signal is compensated by the phase delay as much as the y-direction movement of the target. The phase delay for the range alignment is represented as Eq. (17).

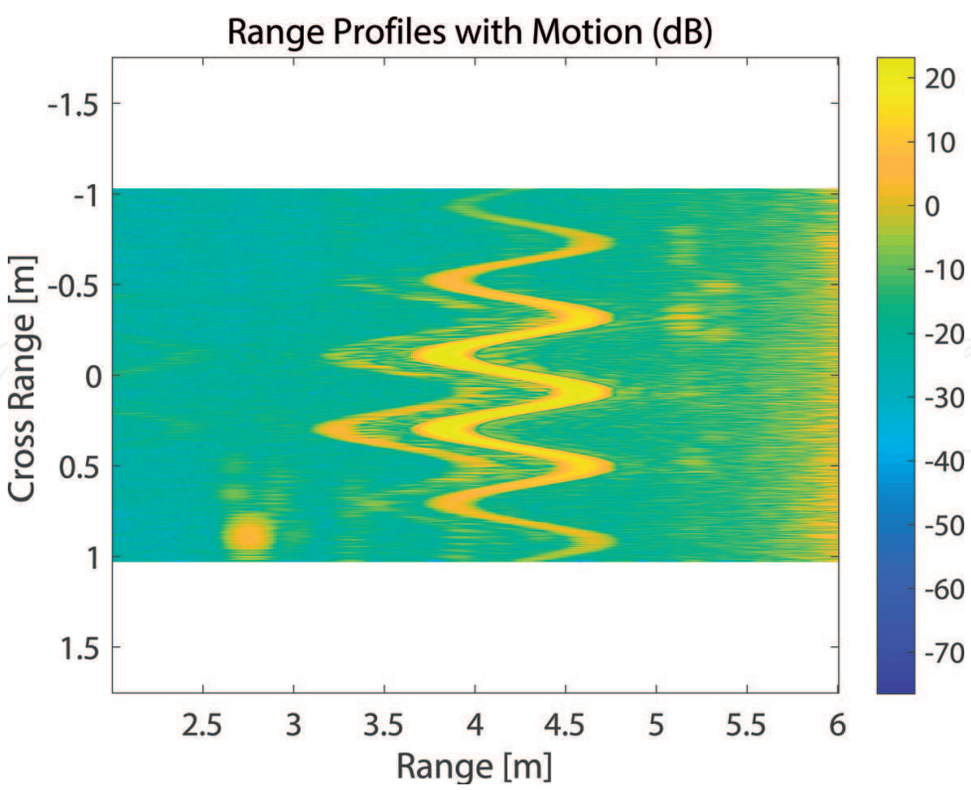

Figure 26. Range profile of a single target with motion.

$$S_{MOCO1}(n_x, n) = e^{-2\pi j\left(\frac{Y_{des}(n)}{dr}\cdot\frac{n_x}{Nx}\right)} \tag{17}$$

where the range cell size is dr, the target movement is Y_{des}, the number of range bins is n_x, and the total number of range bins is N_x.

The compensation of the phase delay calculated by Eq. (17) to the range profile from Eq. (10) can be expressed as Eq. (18). The aligned range profile is expressed as $s_1(f, n)$, and the range profile after applying motion compensation in Eq. (18) is shown in **Figure 27**. As shown in the compensated range profile in **Figure 27**, most of the scatterers are aligned near the range bin.

$$S_1(f, n) = IFFT[s_h(t, n) * S_{MOCO1}(n_x, n)]_t \tag{18}$$

4.2. Phase compensation

The range must be compensated after bin alignment. Using the given motion, the range profile obtained in Eq. (18) can be compensated as Eq. (19).

$$S_2(f, n) = IFFT\left[FFT[S_1(f, n)]_f * e^{-\frac{4\pi j f_0}{c} Y_{des}(n)}\right]_f \tag{19}$$

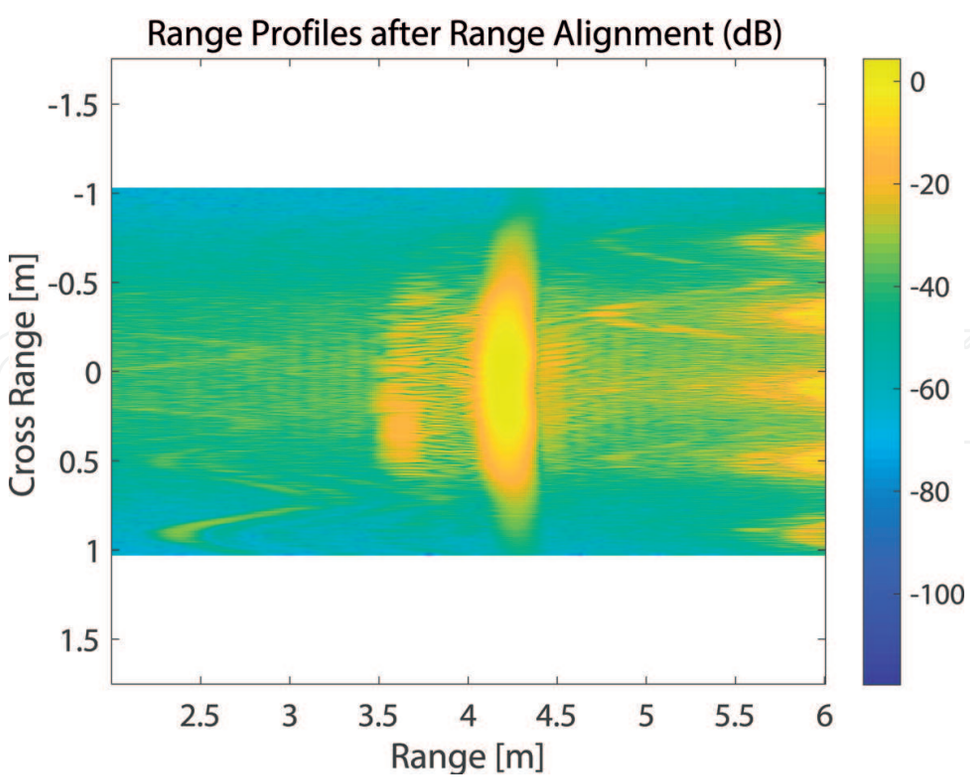

Figure 27. Range profiles after the range bin alignment.

The phase-compensated range profile, $s_2(f, n)$, performs azimuth compression in the same way as SAR imaging without motion. The SAR image can be obtained by performing azimuth compression, as shown in Eq. (20).

$$S_{SAR}(t,n) = IFFT\left[FFT[S_2(f,n)]_n * FFT[S_{MF}(n,y)]_y^*\right]_n \tag{20}$$

The process of motion compensation and SAR imaging can be represented by the flow chart shown in **Figure 28**.

4.3. SAR image after motion compensation

After compensating the motion for the single corner reflector, the SAR image was obtained by azimuth compression. The SAR image is shown in **Figure 29**; the magnitude is in decibel units. The image is depicted in three dimensions in **Figures 30** and **31**. **Figure 32** shows the range direction profile of the SAR image for a point target at a distance of approximately 4.3 m in the range direction. A detailed analysis of **Figure 32** is provided in **Figure 33**.

Table 3 compares and analyzes the resolutions obtained from motion compensation and the general SAR resolution. The motion compensation decreases the level of the peak to side lobe,

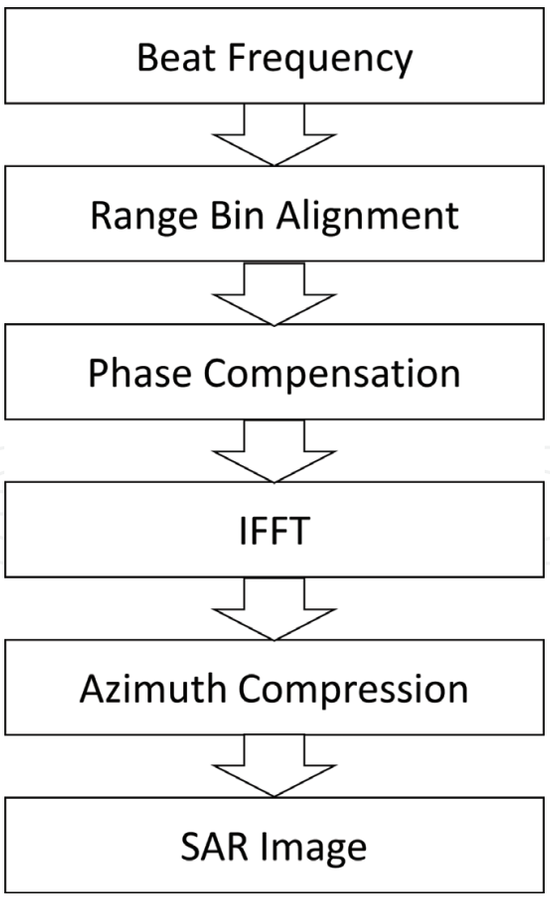

Figure 28. SAR motion compensation block diagram.

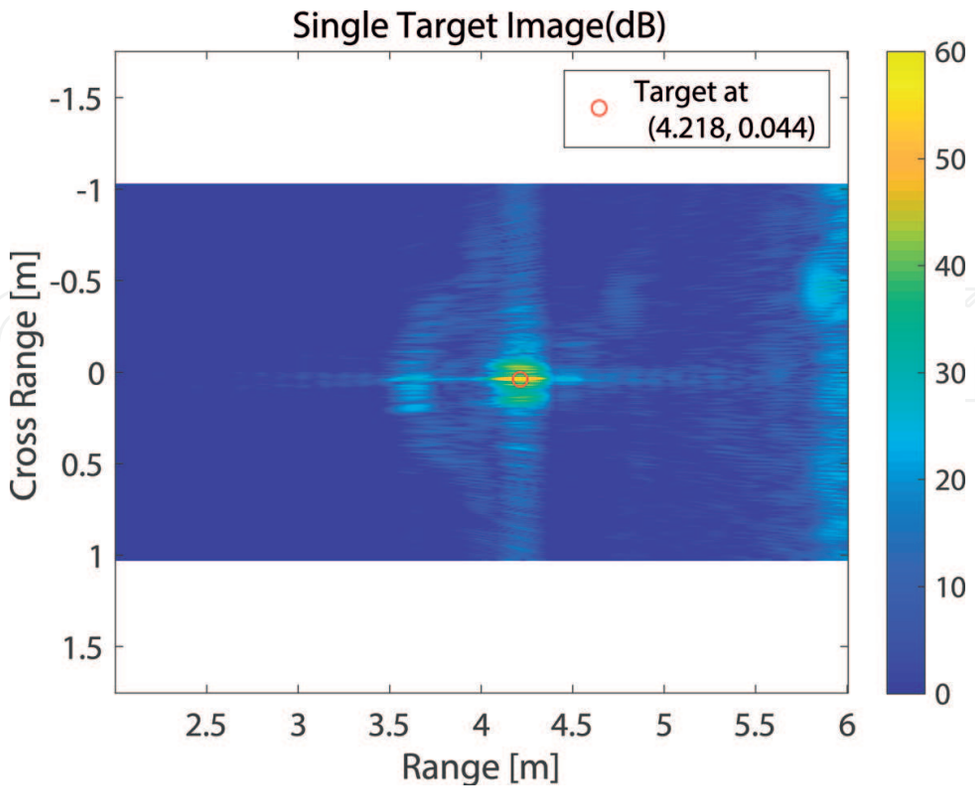

Figure 29. SAR image of the impulse target with motion compensation.

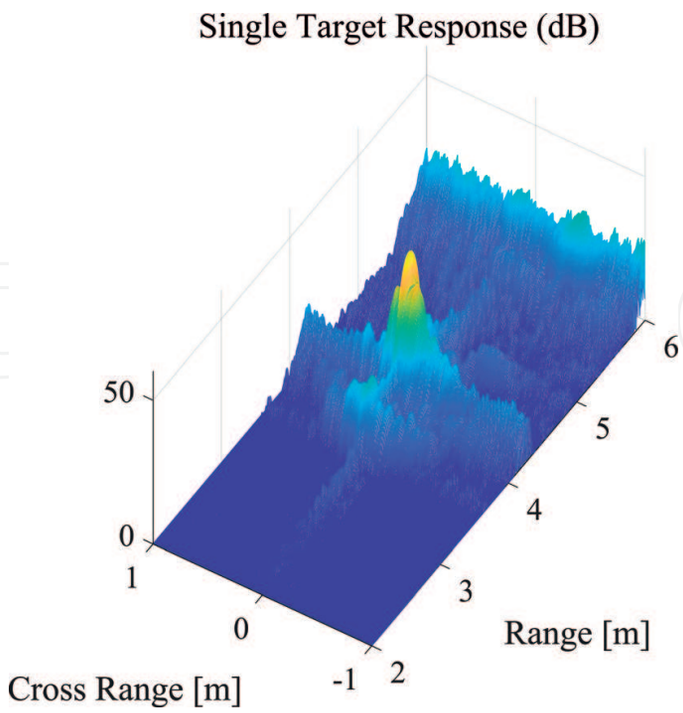

Figure 30. SAR image of the impulse target with motion compensation in three dimensions.

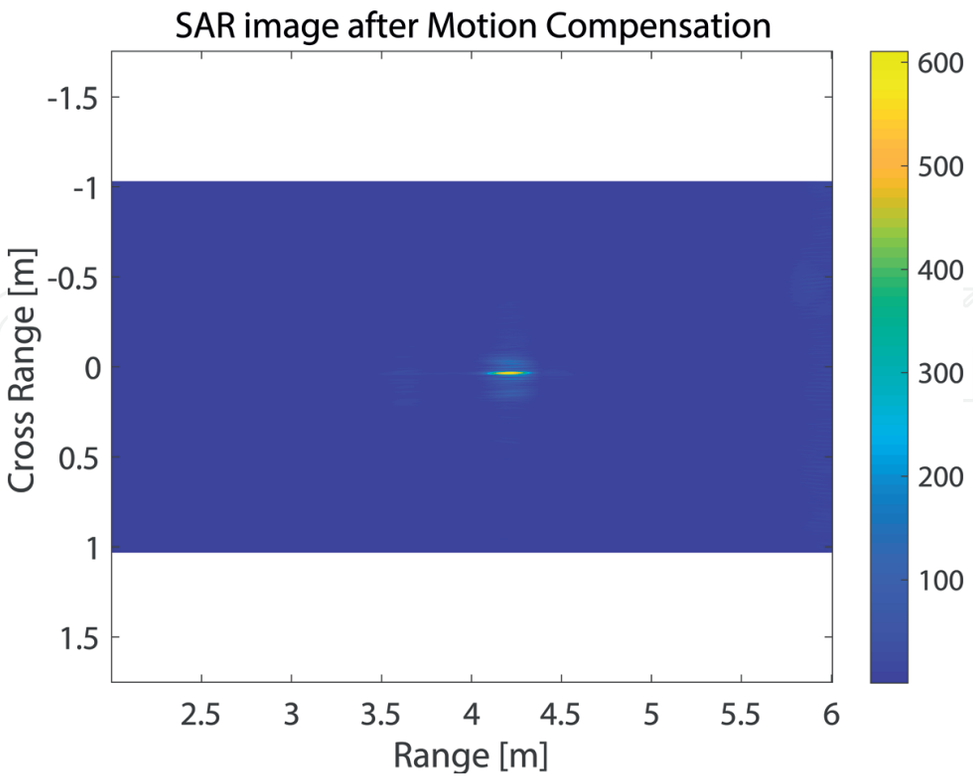

Figure 31. Azimuth-compressed SAR image of the impulse target with motion compensation.

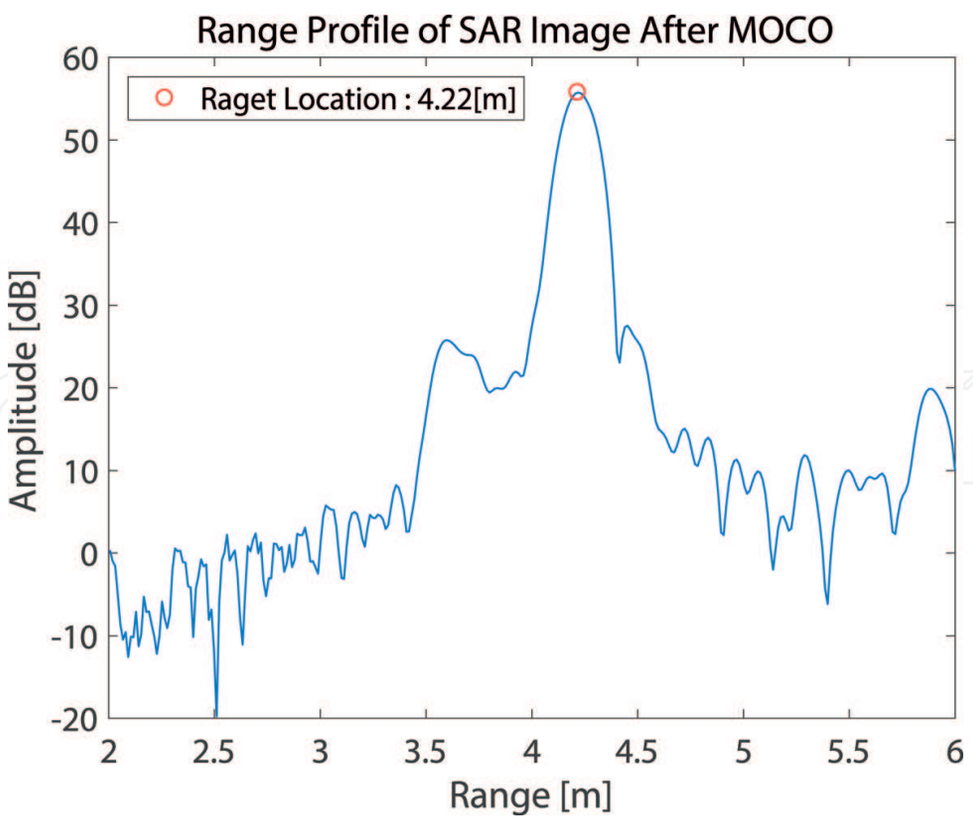

Figure 32. Range profile of the SAR image of the impulse target with motion compensation.

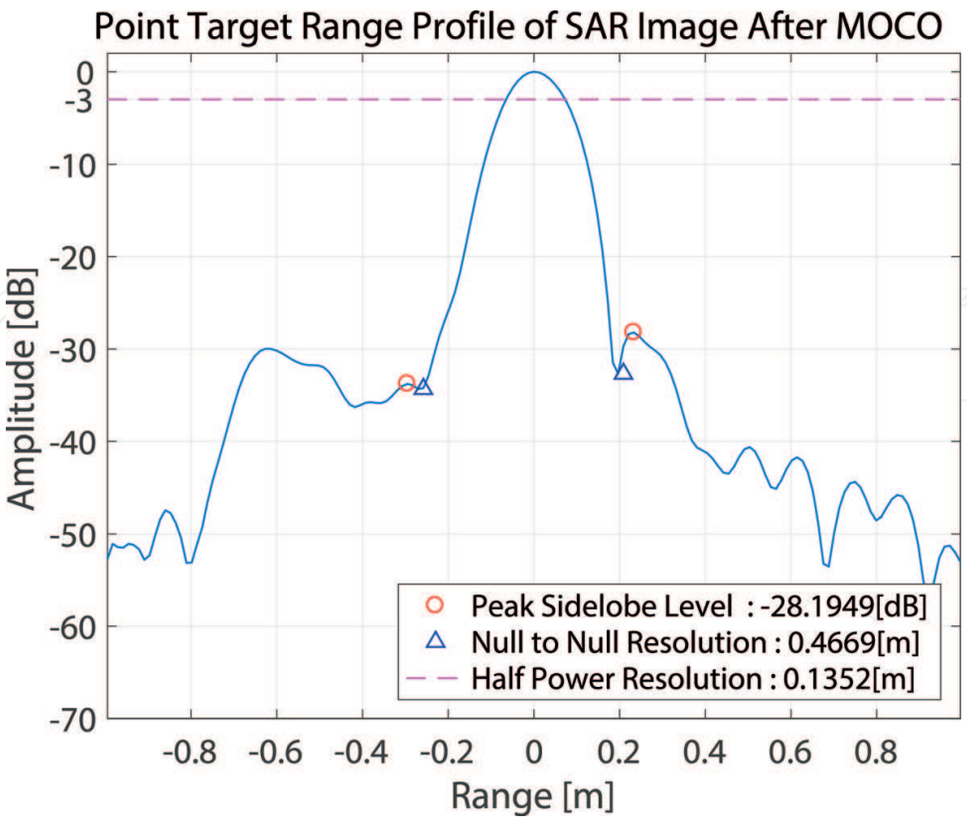

Figure 33. Detailed analysis of the impulse target range profile with motion compensation.

		w/o motion	Motion compensation
Range	Peak side-lobe level	−12.73 dB	−28.1949 dB
	Null-to-null resolution	0.2244 m	0.4669 m
	3-dB resolution	0.0984 m	0.1352 m
Cross-range	Peak side-lobe level	−12.73 dB	−11.22 dB
	Null-to-null resolution	0.0183 m	0.0268 m
	3-dB resolution	0.0076 m	0.0134 m

Table 3. Measured resolution of SAR after motion compensation.

and the resolution in the range direction increases. Furthermore, the resolution in the cross-range direction is degraded.

Furthermore, the cross-range profile at the target range was obtained by taking a column from the SAR image after motion compensation. The cross-range profile with the target location is shown in **Figure 34**. A detailed analysis on the point target is shown in **Figure 35**, including the side-lobe level and resolution.

In addition, experiments with multiple targets were performed as in Section 3.5. The target movement in the range direction was the same as in the above experiment. Three corner

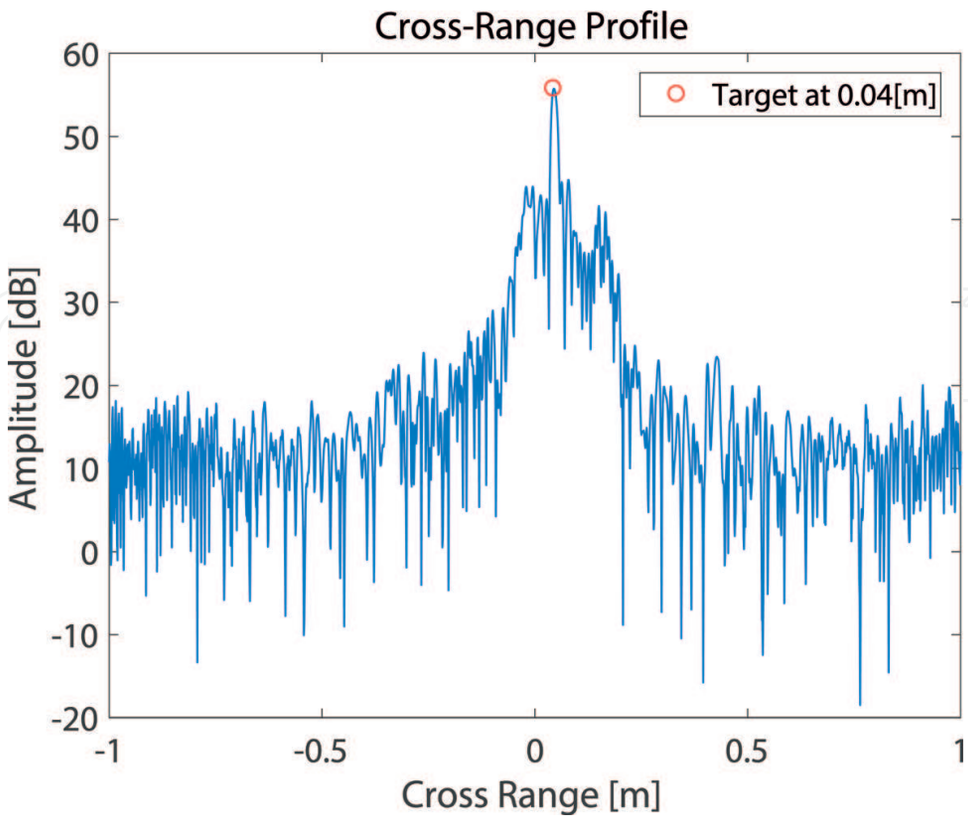

Figure 34. Cross-range profile of the impulse target with motion compensation.

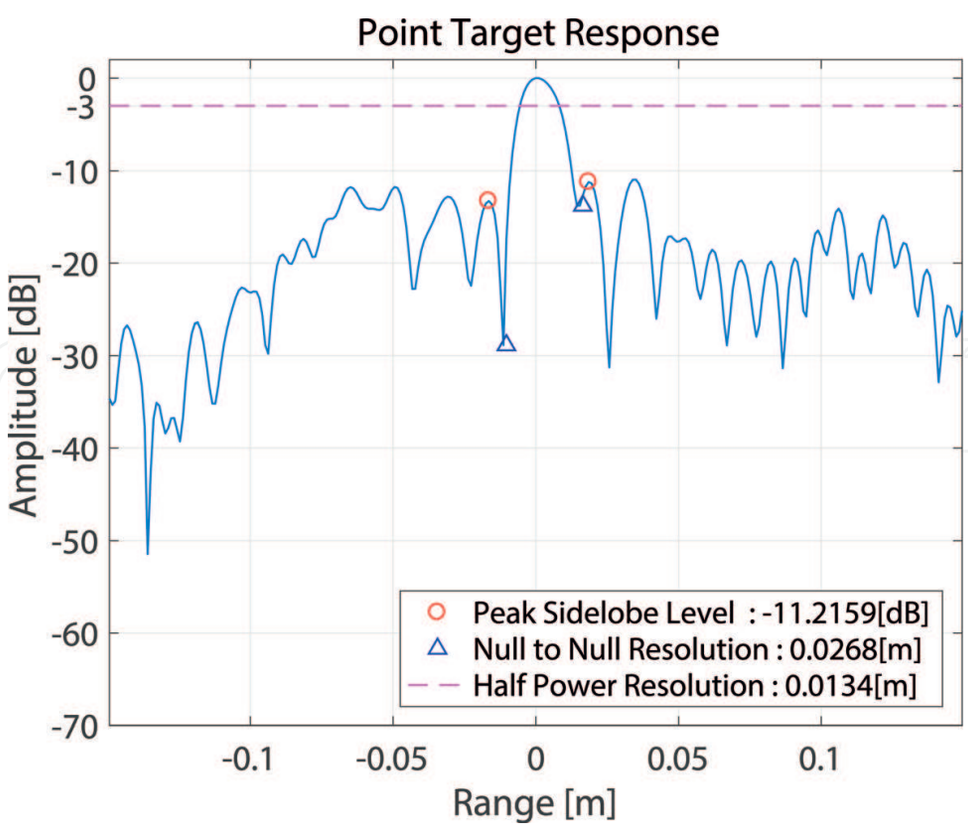

Figure 35. Detailed analysis on the impulse target cross-range profile with motion compensation.

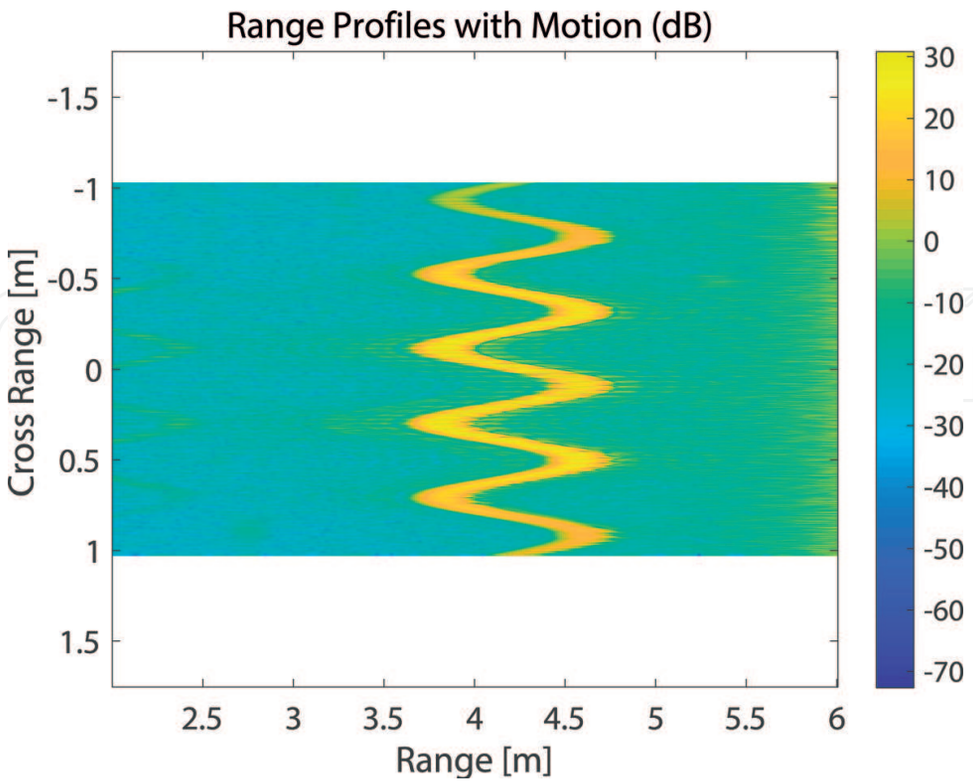

Figure 36. Measured range profile of multiple targets with motion.

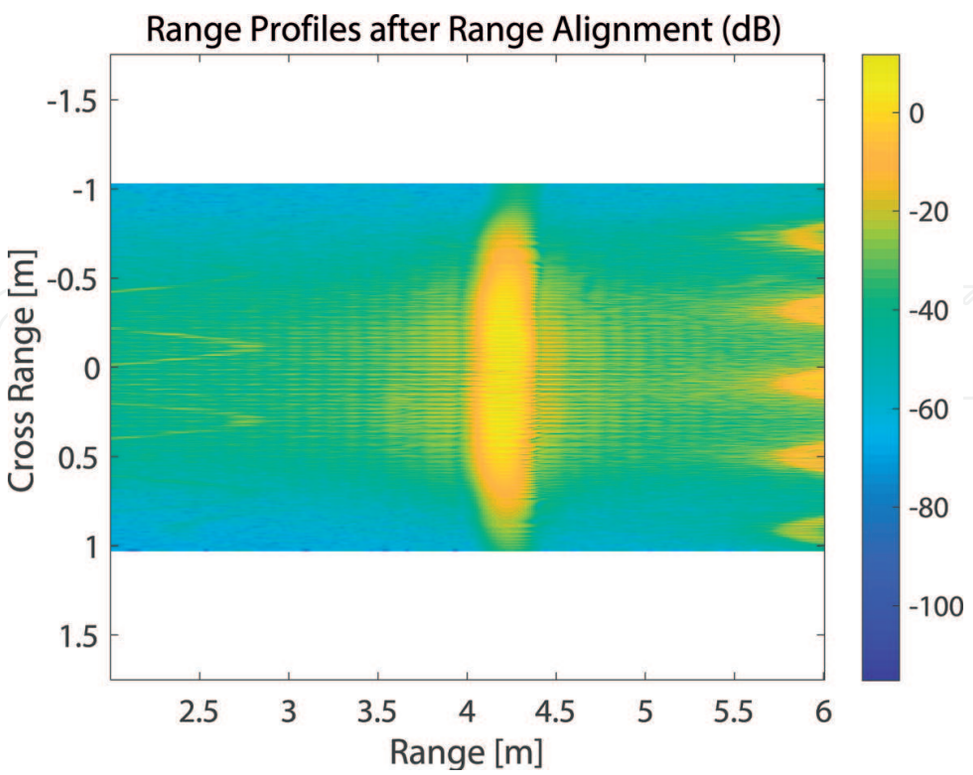

Figure 37. Range profile of multiple targets after range alignment.

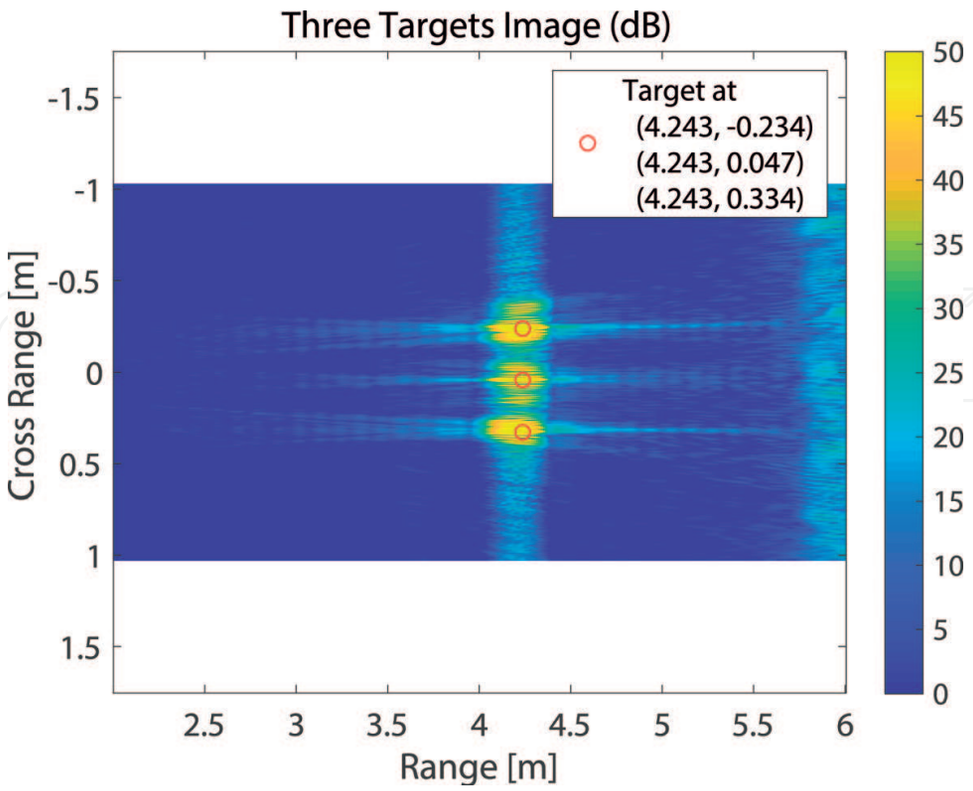

Figure 38. SAR image of multiple targets with motion compensation.

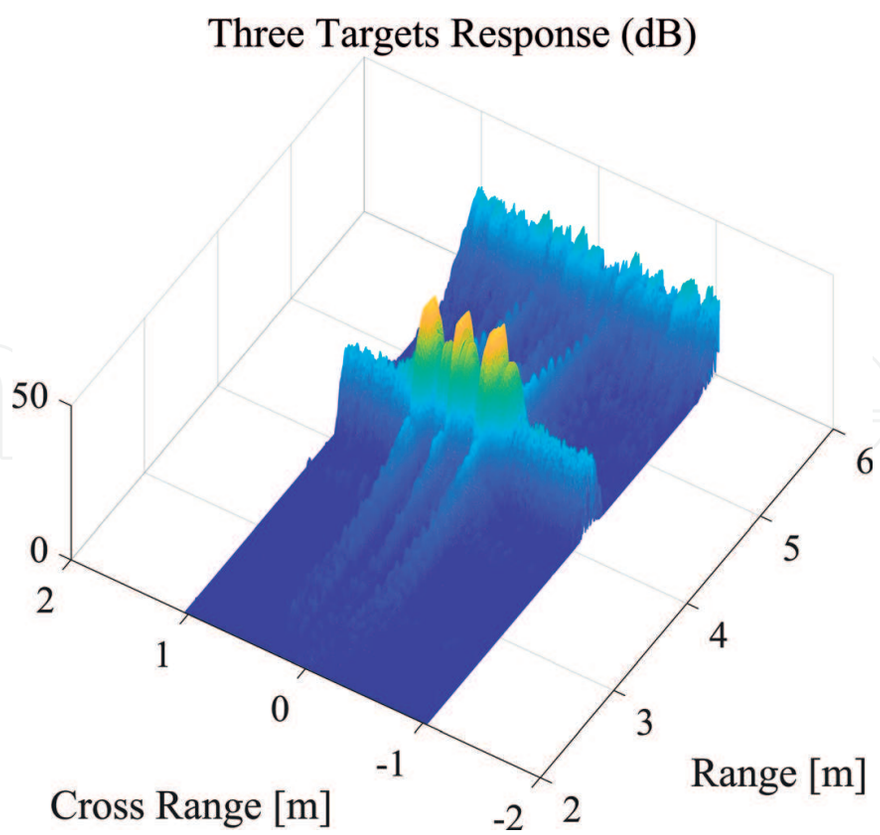

Figure 39. SAR image of multiple targets in three dimensions.

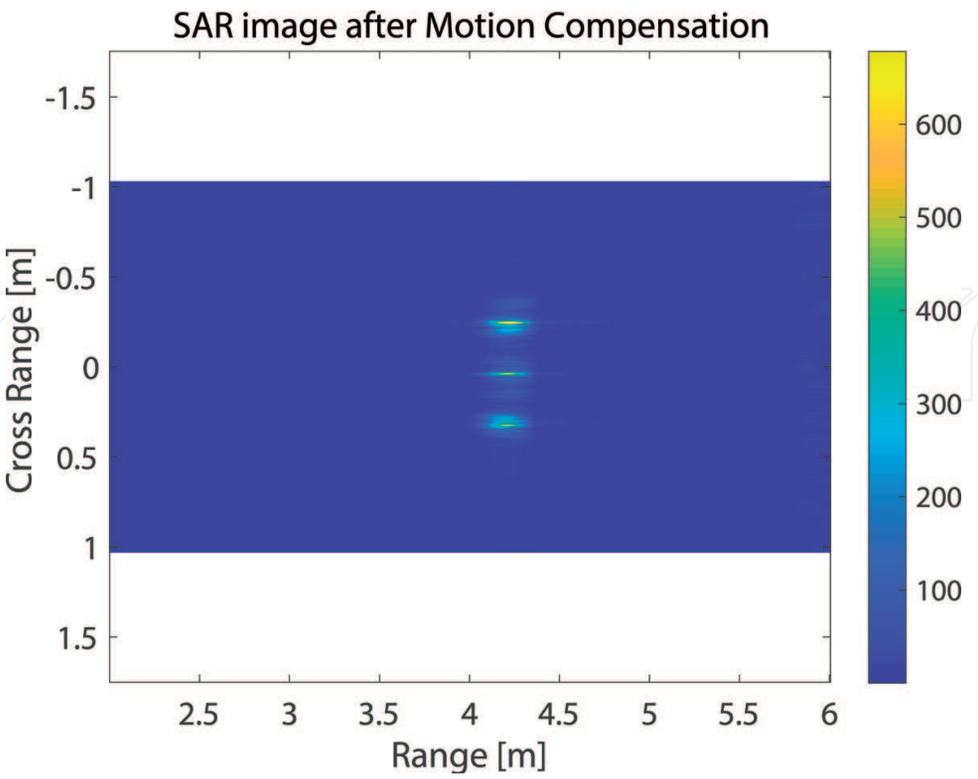

Figure 40. Azimuth-compressed SAR image with motion compensation.

reflectors, which were approximately 0.26 m apart in the azimuth direction and located approximately 4.3 m in the range direction, were used. The range profile is shown in **Figure 36**.

The range profile for the range bin compensation is shown in **Figure 37**. The SAR image for three targets after motion compensation was obtained in decibel units, as shown in **Figure 38**. The three-dimensional SAR image is illustrated in **Figure 39**; the SAR image is depicted in **Figure 40**.

5. Conclusions

A simple SAR algorithm for the W-band and a method for motion compensation of a disturbance-containing signal were presented. A SAR-imaging method in a situation with motion in the range direction was additionally presented. The FMCW radar continuously transmits signals of a predetermined period. If a constant speed along the track is maintained, the moving distance or a period is also maintained. In a conducted experiment, the distance interval was a function of the along-track velocity. With a constant pulse repeat frequency (PRF), the faster the radar is, the longer is the time (or distance) interval between the range profiles. Disturbance of the along-track (azimuth direction) was not considered in this chapter because it can be easily compensated by interpolation. Movement in the range direction has a significant effect on SAR imaging. The proposed method can be used with the exact knowledge of the radar movement.

The described SAR algorithm is based on the RDA with the range variant FM rate. The FMCW radar can be used in a relatively close range and has a low computing cost. In addition, motion compensation can be easily performed using the given position information, even though the RDA method is used. Owing to the W-band characteristics, the RCM can be ignored; however, very precise position information and the motion compensation are required since short wavelengths are used. In the W-band, the beam width is narrow and the synthetic aperture length is short. Therefore, long-term position information is not required; nonetheless, position information that is more precise than the wavelength is required. On account of the short synthetic aperture length, motion may be compensated based on simple parameters. This phenomenon is useful for video SAR because it can increase the frame rate of the SAR image.

Owing to the limitations of navigation sensors, there is a limit to the motion compensation. Precise navigation devices are very expensive and physically difficult to mount on a small aircraft. Therefore, it is necessary to calculate motion and compensate it from received data. In this experiment, although the motor controller had a precision of several millimeters, it was not perfectly compensated by the inaccuracy of the position information. In future studies, the actual flight measurements will be performed and motion compensation will be conducted from the received data. Unlike the experiment in the laboratory, field measurements can be used in the long range. Hence, the SAR algorithm can become more simple, and it is expected to be a real-time-processing approach.

Furthermore, there are many methods for autofocusing based on received data. However, there remains a limit to the autofocusing method. The minimum entropy method is precise as a contrast-based method; however, it has a large computing cost and difficulty in finding the global minimum. With respect to PPP or PGA, there may not be a suitable target in the image, and it is difficult to use in complex structures or extended targets. It may not be particularly suitable for a narrow beam of W-band. Moreover, it is difficult to use in the case wherein the image frame rate is as high as the video SAR.

In this experiment, as a result of the motion compensation, the level of the side lobe was lowered and the resolution of the cross-range was reduced. However, the resolution in the range direction of the SAR image increased. This result requires further investigation and elaborate experimentation. The resolution of the azimuth direction will increase in proportion to the range variation within the synthetic aperture length. Therefore, if motion is exactly known, the azimuth resolution can increase further when there is external motion. Currently, the azimuth resolution is relatively higher than the range resolution. If the resolution is the same for the range and azimuth, and the size of the image is reduced in the azimuth direction, the frame rate can be sufficiently increased.

Experiments in the laboratory are useful for W-band radar development, radar performance validation, and SAR algorithm verification. By using FMCW radar, low power consumption and miniaturization can be achieved. By using high frequency, small antenna and RF devices can be used, which is advantageous when mounting the radar to a flight vehicle. In addition, accurate motion can be applied in the laboratory. However, physical distance constraints exist. Based on the measurements in the laboratory, it was possible to develop W-band

FMCW radar based on FPGA, and the good performance was confirmed. In addition, the SAR algorithm and motion compensation were shown to have good performance in the experiments.

Furthermore, the Hilbert transform returned the component orthogonal to the real component. The Hilbert transform removed symmetric components in the range profile after the IFT. This is useful when only the real component is received in the FMCW radar. However, it should be used when I and Q data are not actually received.

In this chapter, the development of a high-resolution W-band radar based on FPGA is described, and W-band SAR images can be obtained via the motion compensation. The motion compensation method in W-band has been described as accurate phase compensation. As a result, the SAR images are obtained in the laboratory using developed W-band radar, and the SAR images are consistent with the theoretical resolution. Although the resolution of the SAR image is slightly lower than that of the motion compensation, the SAR image can be obtained almost the same as the theory.

Acknowledgements

This research was supported by the MSIT (Ministry of Science and ICT), Korea, under the ICT Consilience Creative program (IITP-2017-2017-0-01015) supervised by the IITP (Institute for Information & Communications Technology Promotion), the Civil Military Technology Cooperation Program, and the Institute for Information & Communications Technology Promotion (IITP) grant funded by the Korea government (MSIT) (2017–0-00678, A Development of SAR for small-sized UAV).

Author details

Jiwoong Yu[1,2]*, Sumin Kim[1] and Min-Ho Ka[1]

*Address all correspondence to: jiwoong.yu@yonsei.ac.kr

1 School of Integrated Technology, Yonsei Institute of Convergence Technology, Yonsei University, South Korea

2 Satellite Technology Research Center, Korea Advanced Institute of Science and Technology, South Korea

References

[1] Moreira A et al. A tutorial on synthetic aperture radar. IEEE Geoscience and Remote Sensing Magazine. 2013;**1**(1):6-43

[2] Yu J, Dewantari A, Ka M-H. Measurement of the rotation center from the received signals for ultrahigh-resolution radar imaging. IEEE Antennas and Wireless Propagation Letters. 2017;**16**:2266-2269

[3] Yu J, Ka M-H. Precision near-field reconstruction in the time domain via minimum entropy for ultra-high resolution radar imaging. Remote Sensing. 2017;**9**(5):449

[4] Kim S, Yu J, Jeon SY, Dewantari A, Ka M-H. Signal processing for a multiple-input, multiple-output (MIMO) video synthetic aperture radar (SAR) with beat frequency division frequency-modulated continuous wave (FMCW). Remote Sensing. 2017;**9**(5):491

[5] Metasensing. Airborne Sar [Online]. Available: http://www.metasensing.com/wp/index.php/products/airborne-sar/minisar-sensor/

[6] ImSAR. Imsar's Collision-Avoidance Radar for Small Uas Expected to be Available Late 2016, [Online]. Available: http://www.imsar.com/pages/news.php?article = imsars collisionavoidance radar for small uas expected to be available late; 2016

[7] Raney RK, Cahill JT, Patterson G, Bussey DBJ. The m-chi decomposition of hybrid dual-polarimetric radar data. In: Geoscience and Remote Sensing Symposium (IGARSS), 2012 IEEE International. IEEE; 2012. pp. 5093-5096

[8] Sakai F, Suzuki H, Sato H, Sawaya K, Mizuno K. High resolution millimeter-wave imaging radar using inline tx/rx antennas. In: Radar Conference, 2008, EuRAD 2008. European, IEEE; 2008. pp. 156-159

[9] Goshi D, Liu Y, Mai K, Bui L, Shih Y. Recent advances in 94 ghz fmcw imaging radar development. In: Microwave Symposium Digest, 2009, MTT'09. IEEE MTT-S International, IEEE; 2009. pp. 77-80

[10] Palm S, Wahlen A, Stanko S, Pohl N, Wellig P, Stilla U. Real-time onboard processing and ground based monitoring of fmcw-sar videos. In EUSAR 2014; 10th European Conference on Synthetic Aperture Radar; Proceedings of, VDE; 2014. pp. 1-4

[11] Meta A, Hoogeboom P, Ligthart LP. Signalprocessingforfmcw sar. Geoscience and Remote Sensing, IEEE Transactions. 2007;**45**(11):3519-3532

[12] Ribalta A. Time-domain reconstruction algorithms for fmcw-sar. Geoscience and Remote Sensing Letters, IEEE. 2011;**8**(3):396-400

[13] SAGE Millimeter, SAR-2507-10-S2. [Online]. Available from: https://www.sagemillimeter.com/content/datasheets/SAR-2507-10-S2.pdf

[14] Xilinx, Zynq-7000 All Programmable SoC Data Sheet: Overview, [Online]. Available from: https://www.xilinx.com/support/documentation/data_sheets/ds190-Zynq-7000-Overview.pdf

[15] Charvat GL, Kempel LC. Synthetic aperture radar imaging using a unique approach to frequency-modulated continuous-wave radar design. Antennas and Propagation Magazine, IEEE. 2006;**48**(1):171-177

[16] Charvat GL, Kempell LC, Coleman C. A low-power high- sensitivity x-band rail sar imaging system [measurement's corner]. Antennas and Propagation Magazine, IEEE. 2008;**50**(3):108-115

[17] Xi L, Guosui L, Ni J. Autofocusing of isar images based on entropy minimization. IEEE Transactions on Aerospace and Electronic Systems. 1999;**35**(4):1240-1252

[18] Giusti E, Martorella M. Range doppler and image autofocusing for fmcw inverse synthetic aperture radar. IEEE Transactions on Aerospace and Electronic Systems. 2011;**47**(4):2807-2823

[19] Berizzi F, Corsini G. Autofocusing of inverse synthetic aperture radar images using contrast optimization. IEEE Transactions on Aerospace and Electronic Systems. 1996;**32**(3): 1185-1191

[20] Wahl D, Eichel P, Ghiglia D, Jakowatz C Jr. Phase gradient autofocus-a robust tool for high resolution sar phase correction. IEEE Transactions on Aerospace and Electronic Systems. 1994;**30**(3):827-835

[21] Otten MPG, Van Rossum WL, Van Bree RJP. Extended pga for range migration algorithms. IEEE transactions on Aerospace and electronic systems. 2006;**42**(2):478-488

[22] Werness S, Carrara W, Joyce L, Franczak D. Moving target imaging algorithm for sar data. IEEE Transactions on Aerospace and Electronic Systems. 1990;**26**(1):57-67

[23] Dungan KE, Nehrbass JW. Wide-area wide-angle sar focusing. Aerospace and Electronic Systems Magazine, IEEE. 2014;**29**(1):21-28

[24] Chen C-C, Andrews HC. Target-motion-induced radar imaging. IEEE Transactions on Aerospace and Electronic Systems. 1980;(1):2-14

[25] Cao P, Xing M, Sun G, Li Y, Bao Z. Minimum entropy via subspace for isar autofocus. Geoscience and Remote Sensing Letters, IEEE. 2010;**7**(1):205-209

[26] Wallace H, Gorman J, Maloney P. Video Synthetic Aperture Radar (Visar); 2012

[27] Johannes W, Stanko S, Wahlen A, Sommer R, Pohl N, Wellig P, Sennhauser C, Meier E, Kallfass I. Implementation of a 35 ghz sar sensor and a high resolution camera to enable real-time observation. In: EUSAR 2014; 10th European Conference on Synthetic Aperture Radar; Proceedings of, pp. 1-4, VDE. 2014

[28] Doerry AW, Dubbert DF, Thompson M, Gutierrez VD. A portfolio of fine resolution ka-band sar images: Part i. In: Defense and Security, pp. 13–24, International Society for Optics and Photonics. Proceedings of SPIE. Vol. 5788. Bellingham, WA: SPIE; 2005

[29] Avnet. ZedBoard Hardware User's Guide [Online]. Available from: https://reference.digilentinc.com/_media/zedboard:zedboard_ug.pdf

[30] Charvat GL. Small and short-range radar systems. Boca Raton, FL: Taylor & Francis Group, CRC Press; 2014

[31] IMST GmbH imst radar -small and flexible 24 ghz radar modules. http://www.radar-sensor.com/?navanchor = 2,110,039. [Accessed: April 07, 2017]

[32] Infineon Technologies AG 24ghz rdar - industrial. https://www.infineon.com/cms/en/product/rf-and-wireless-control/mmwave-mmic/24-ghz-radar-industrial/channel.html?channel = 5546d46145f1f3a40146140e9c1c1956. [Accessed: April 07, 2017]

[33] SIVERS IMA fmcw Radar Sensors fron end, 24 ghz to 77 ghz-sivers ima. https://siversima.com/products/radar-sensors/. [Accessed: April 07 2017]

[34] InnoSenT Application of Radar Systems. http://www.innosent.de/en/applications/. [Accessed: April 07, 2017]

[35] Mahafza BR. Radar signal analysis and processing using MATLAB. New York: Taylor & Francis Group, CRC Press; 2016

[36] Richards MA. Fundamentals of signal processing to fundamentals of radar signal processing, USA. pp. 171-183, 581-582; 2015

[37] Ozdemir C. Inverse Synthetic Aperture Radar Imaging with Matlab Algorithms. Wiley; 2012. pp. 139-140

[38] Moreira A, Huang Y. Airborne SAR processing of highly squinted data using a chirp scaling approach with integrated motion compensation. IEEE Transactions on Geoscience and Remote Sensing. 1994;**32**(5):1029-1040

[39] Fornaro G, Franceschetti G, Perna S. On center-beam approximation in SAR motion compensation. IEEE Geoscience and Remote Sensing Letters. 2006;**3**(2):276-280

[40] Xing M et al. Motion compensation for UAV SAR based on raw radar data. IEEE Transactions on Geoscience and Remote Sensing. 2009;**47**(8):2870-2883

[41] Buckreuss S. Motion compensation for airborne SAR based on inertial data, RDM and GPS. Geoscience and Remote Sensing Symposium, 1994. IGARSS'94. Surface and Atmospheric Remote Sensing: Technologies, Data Analysis and Interpretation., International. Vol. 4. IEEE; 1994

[42] Carrara R, Goodman R. Spotlight Synthetic Aperture Radar: Signal Processing Algorithms. Norwood, MA: Artech House; 1995

[43] Cumming IG, Wong FH. Digital processing of synthetic aperture radar data. Artech house 1.2.2005: 3